FAST SIMULATION AND MODELING OF SCATTERING FROM TARGETS
IN MIMO IMAGING SYSTEMS

A THESIS SUBMITTED TO
THE GRADUATE SCHOOL OF NATURAL AND APPLIED SCIENCES
OF
MIDDLE EAST TECHNICAL UNIVERSITY

BY

YUNUS EMRE GÜL

IN PARTIAL FULFILLMENT OF THE REQUIREMENTS
FOR
THE DEGREE OF MASTER OF SCIENCE
IN
ELECTRICAL AND ELECTRONIC ENGINEERING

MAY 2022

Approval of the thesis:

**FAST SIMULATION AND MODELING OF SCATTERING FROM
TARGETS IN MIMO IMAGING SYSTEMS**

submitted by **YUNUS EMRE GÜL** in partial fulfillment of the requirements for the
degree of **Master of Science** in **Electrical and Electronic Engineering, Middle
East Technical University** by,

Prof. Dr. Halil Kalıpçılar
Dean, Graduate School of **Natural and Applied Sciences**   _____

Prof. Dr. İlkay Ulusoy
Head of the Department, **Electrical and Electronic Eng.**   _____

Assoc. Prof. Dr. Lale Alatan
Supervisor, **Electrical and Electronic Eng., METU**   _____

Examining Committee Members:

Prof. Dr. Sencer Koç
Electrical and Electronic Eng., METU   _____

Assoc. Prof. Dr. Lale Alatan
Electrical and Electronic Eng., METU   _____

Prof. Dr. Özlem Aydın Çivi
Electrical and Electronic Eng., METU   _____

Prof. Dr. Özgür Ergül
Electrical and Electronic Eng., METU   _____

Prof. Dr. Özlem Özgün
Electrical and Electronic Eng., Hacettepe University   _____

Date: 11.05.2022

I hereby declare that all information in this document has been obtained and presented in accordance with academic rules and ethical conduct. I also declare that, as required by these rules and conduct, I have fully cited and referenced all material and results that are not original to this work.

Name Last name : Yunus Emre Gül

Signature :

ABSTRACT

FAST SIMULATION AND MODELING OF SCATTERING FROM TARGETS IN MIMO IMAGING SYSTEMS

Gül, Yunus Emre
Master of Science, Electrical and Electronic Engineering
Supervisor: Assoc. Prof. Dr. Lale Alatan

May 2022, 86 pages

The forward model analysis in a multiple input multiple output (MIMO) system requires the computation of the signals received by receiver antennas when various targets are illuminated by a transmitter antenna. The full wave analysis of such systems provides accurate results with high computational cost. Fast analysis of the system can be achieved by simple models based on several approximations which limits the accuracy. In this thesis, a modeling technique that provides better accuracy compared to simple models and achieves faster simulation time than full-wave analysis of the whole system is proposed. Full-wave simulation result of an isolated antenna is used as an input for this methodology. With the help of surface equivalence theorem and small dipole approximation, the incident field over the target and receiver antennas are found. MoM technique is employed to find scattered fields created by target due to this incident field. Finally, scattered field data is utilized in reaction theorem to compute the signal received by the receiver antenna.

Keywords: MIMO, Method of Moments, Reaction Theorem

ÖZ

ÇGÇÇ GÖRÜNTÜLEME SİSTEMLERİNDEKİ HEDEFLERİN SAÇILMASININ HIZLI BENZETİMİ VE MODELLENMESİ

Gül, Yunus Emre
Yüksek Lisans, Elektrik ve Elektronik Mühendisliği
Tez Yöneticisi: Doç. Dr. Lale Alatan

Mayıs 2022, 86 sayfa

Çok-giriş-çok-çıkış (ÇGÇÇ) sistemindeki ileri çözüm analizi, verici anten tarafından aydınlatılan hedeften alıcı antene gelen işaretin hesaplanmasına ihtiyaç duymaktadır. Bu tip sistemlerin tam dalga analizi doğru sonuçları yüksek hesaplama maliyeti ile sağlamaktadır. Sistemin hızlı analizi doğruluğu sınırlayan birkaç yaklaşım kullanılarak gerçekleştirilebilir. Bu tezde basit modellerle daha yüksek doğrulukta ve tüm sistemin tam dalga analizinden daha hızlı benzetim süresine sahip bir modelleme tekniği önerilmiştir. Bu metodoloji için, izole edilmiş bir antenin tam dalga benzerim sonucu girdi olarak kullanılmıştır. Yüzey denklik teoremi ve küçük dipol yaklaşımı sayesinde, hedef ve alıcı antenler üzerine gelen dalgalar bulunmuştur, Momentler metodu tekniği hedeften saçılan gelen dalgadan dolayı oluşan saçılma dalgalarını bulmak için kullanılmıştır. Son olarak, saçılan dalga verisi, tepki teoremi dahilinde kullanılarak alıcı antenden alınan işaretin hesaplanmasında kullanılmıştır.

Anahtar Kelimeler: ÇGÇÇ, Momentler Yöntemi, Tepki Teoremi

To My Family

ACKNOWLEDGMENTS

TABLE OF CONTENTS

LIST OF TABLES

TABLES

LIST OF FIGURES

FIGURES

LIST OF ABBREVIATIONS

ABBREVIATIONS

DDM: Domain Decomposition Method

EFIE: Electric Field Integral Equation

MFIE: Magnetic Field Integral Equation

MIMO: Multiple Input Multiple Output

MoM: Method of Moments

PEC: Perfect Electric Conductor

PMC: Perfect Magnetic Conductor

RWG: Rao-Wilton-Glisson

CHAPTER 1

INTRODUCTION

In the last two decades, several multiple-input multiple output (MIMO) imaging systems are developed for security [1], [2] and biomedical applications [3], [4] .

In MIMO imaging systems, transmitter antennas and receiver antennas may be separated from each other as shown in Figure 1.1. Transmitter antennas radiate one at a time and the signals received by each receiver antenna are recorded. If the number of transmitter and receiver antennas are defined by N_{tx} and N_{rx} respectively, $N_{\text{tx}} \times N_{\text{rx}}$ number of signals are processed to construct the image in the imaging domain. Depending on the application, transmitter and receiver antennas may be placed on a planar surface, as in concealed weapon detection radars, or on the surface of a hemisphere or cylinder as in brain imaging systems.
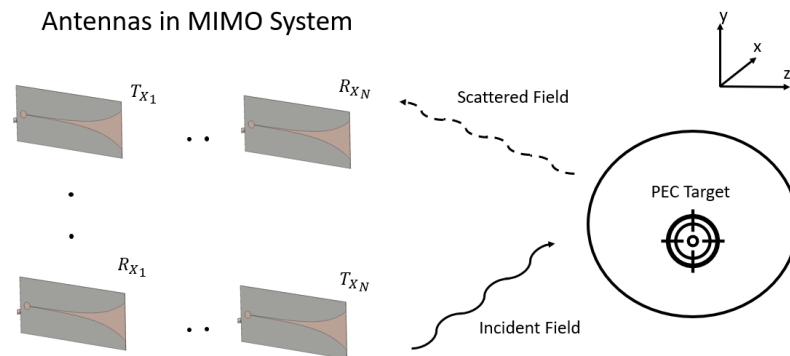
Figure 1.1 A MIMO system with separate antenna sets for transmitting and receiving

In order to optimize the number of antennas and their locations to obtain best imaging performance with least complexity, the MIMO system needs to be modeled and

simulated for different target in the imaging domain. For this forward model analysis, both simple models that provide rapid results with limited accuracy and rigorous models that yield accurate results with high computational cost are available. For example, one of these simple models makes an assumption that, all the antennas in the system radiates isotropically, so that they are radiating equally at all directions. Then it assumes only point scatterers and scattered fields are computed by assuming the reflectivity of the scatterer to be 1 and neglecting multiple scattering.

On the other hand, full-wave simulations can give very accurate results since they model the system rigorously. However, full-wave simulation of a system that includes whole MIMO array and the target is computationally expensive and has large memory requirements. But, during the design process, electromagnetic simulation may need to be run several times to find optimal configuration for the array. This leads to impractical simulation times which again proves to be not feasible for initial design phase.

The aim of this thesis is to propose an analysis method that has a good balance between accuracy and computational cost. To decrease the computational cost of the full-wave analysis of the whole system together with the target, full-wave analysis of transmitter antenna, receiver antenna and the scattering from the target are performed separately. Then, the fields calculated by those separate full-wave analysis are combined by making use of the field equivalence and reaction theorems.

The proposed approach can be summarized as follows:

1. The full-wave analysis of a single isolated transmitter antenna is performed by using a commercially available electromagnetic simulator CST Microwave Studio. Fields radiated by the antenna on the surface of a rectangular prism shaped box that encloses the antenna are exported as it is shown in Figure 1.2.

2. From the exported fields of the transmitter antenna, incident field on the target is computed. A Method of Moments (MoM) based software is developed to compute the fields scattered by the target.

3. The fields scattered by the target are computed on the surface of a rectangular prism shaped box that encloses the receiver antenna as it is shown in Figure 1.2.

4. Since same antennas are used as transmitter and receiver, the exported fields in the first step will be same for the receiver antenna. To compute the open circuit voltage at the receiver antenna, reaction theorem is used and inner product of the fields radiated by the antenna and the fields scattered by the target is computed over the box enclosing receiver antenna.
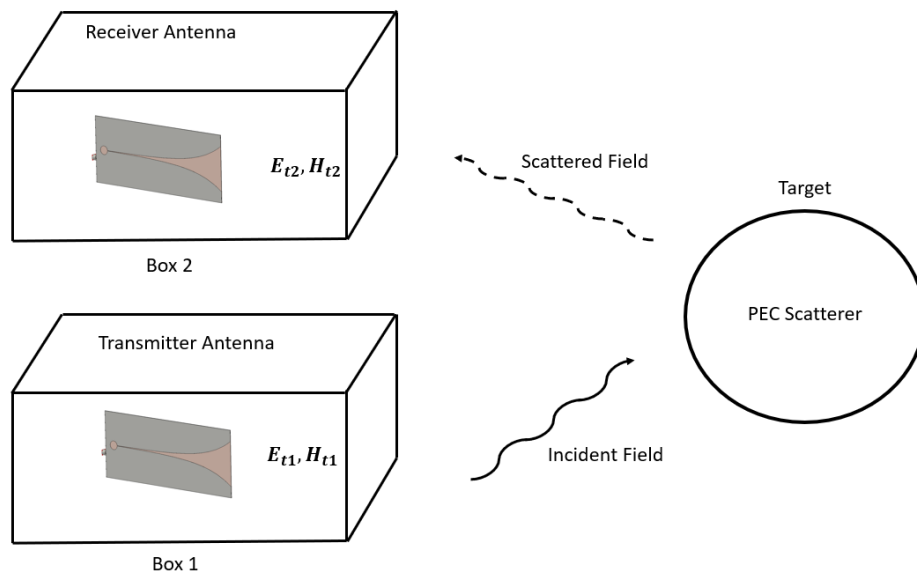
Figure 1.2 Proposed Method for analyzing MIMO systems

Since each antenna and scatterer are analyzed by full-wave methods, the accuracy is considerably improved compared to simple models. The only source of error in the proposed approach is assuming that an antenna radiates into free space and neglecting the fields scattered by other antennas and the target. Through simulation results it will be demonstrated in this thesis that; this assumption does not introduce a significant deterioration in accuracy. However, this assumption significantly decreases the computational cost of analysis. When the full-wave analysis of the whole system is performed all transmitter and receiver antennas and the target needs to be discretized and it results in a large number of unknowns. On the other hand, in

the proposed approach only one antenna is discretized in first step of the method and then only the target is discretized in the second step. As a result, the number of unknowns is reduced significantly. That translates into a significant reduction in computation time.

The proposed method can be classified as a domain decomposition method (DDM) where full-wave analyses are performed in smaller subdomains of the whole simulation model and then their results are combined by using the boundary conditions on the surfaces of subdomains. However, it is different than the DDMs proposed in literature, [5]–[11]. In literature, domain decomposition is utilized either to combine two different full-wave analysis methods as in [5] and [6] or to hybridize a full-wave analysis method with an asymptotic high frequency method as in [7]–[9]. For example, in [5], Finite Element Method is used to model the domain that contains inhomogeneities whereas MoM is utilized in open radiating homogenous regions. On the other, when analyzing antennas on electrically large platforms ([7]–[9]) antenna is enclosed by a fictitious box. Then MoM or Finite Difference Time Domain method is used to model the antenna and asymptotic high frequency techniques like physical optics or shooting and bouncing ray method is utilized to model the scattering from the platform.

In all of these DDMs, either a large matrix equation that matches the field values on the surface of the subdomains are solved or the fields on these surfaces are computed iteratively by solving smaller problems successively. Hence the exact solutions on the surfaces of the domains are computed. However, in this thesis, approximations are made to reduce the computational cost. Therefore, the domain decomposition method proposed in this work does not provide an accuracy as high as other DDMs available in literature.

The use of reaction theorem to compute the coupling between two antennas mounted on a large platform, [12]–[14] or between an antenna and a circuit in the near-field of the antenna [15] is proposed in literature. However, these studies do not consider scattering from a target. Only in [12], the coupling between two antennas is studied

4

in the presence of a metal pole with a plate between antennas. But a difference of about 1 to 2 dB is reported between measured and computed results. Hence a good accuracy could not be achieved. This thesis work can be considered as the extension of those studies available in literature since it also considers scattering from a target in addition to coupling between antennas.

In Chapter 2, first the procedure to export the fields of transmitter antenna from CST Microwave Studio is explained. Then the method to compute the incident field over the target and directly coupled fields to receiver antenna by using the exported fields is presented.

In Chapter 3, computation of the scattered fields from the target by using MoM is explained.

In Chapter 4, a review of reaction theorem is presented and then its application in the proposed model is explained.

Finally, in Chapter 5 conclusion of this work is given and brief discussion on the strong and weak sides of the proposed method compared to the full-wave analysis of the whole system is provided.

CHAPTER 2

CALCULATION OF INCIDENT FIELDS TO THE TARGET BY USING THE RADIATED FIELDS OF TRANSMITTER ANTENNA

In this chapter, aim is to determine the electromagnetic fields at the position of receiver antennas and at the position of a single target, by using full-wave simulation. This scenario contains a single transmitter and results of a single isolated antenna over a surface that encloses the antenna are computed. Fields over that surface are also used in Chapter 4 while utilizing the reaction theorem.

Once the electromagnetic fields are known over a surface that encloses the antenna, fields created by that antenna can be found by using surface equivalence theorem.

Surface equivalence theorem is a principle based on defining equivalent sources over an arbitrary closed surface such that they produce same fields outside of the closed surface that actual sources inside the surface would excite. It states that if the tangential electric field intensity and magnetic field intensity over a closed surface is known entirely, then fields outside of the closed surface can be determined [16] as shown in Figure 2.1 to create an equivalent problem that yields same results, sources in equivalent surface is removed and following equivalent current densities over the closed surfaces are defined by enforcing boundary conditions.

$$\bar{J}_S = \hat{n} \times (\bar{H}_1 - \bar{H}) \tag{2.1}$$

$$\bar{M}_S = -\hat{n} \times (\bar{E}_1 - \bar{E}) \tag{2.2}$$
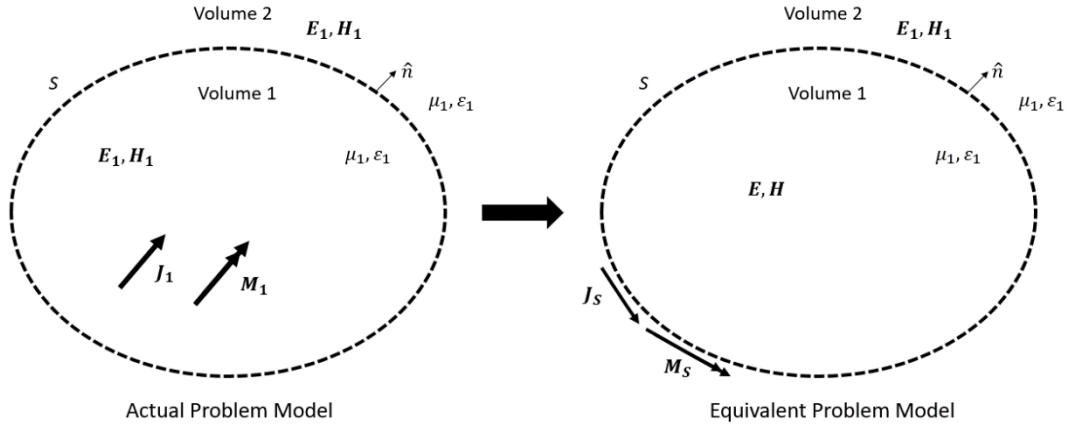
Figure 2.1 Transition from Actual Problem to Equivalent Problem

$\bar{J}_S$ and $\bar{M}_S$ are equivalent electric and magnetic current densities respectively, $\bar{H}_1$ $(\bar{E}_1)$ is the magnetic (electric) field outside of the closed surface (Volume 2) and $\bar{H}$ $(\bar{E})$ are the magnetic (electric) fields inside of the closed surface (Volume 1). For the sake of simplicity fields in Volume 1 can be chosen to be equal to zero [17].

For the null fields inside S, boundary conditions can be rearranged as following:

$$\bar{J}_S = \hat{n} \times (\bar{H}_1 - \bar{H})|_{\bar{H}=0} = \hat{n} \times \bar{H}_1 \qquad (2.3)$$

$$\bar{M}_S = -\hat{n} \times (\bar{E}_1 - \bar{E})|_{\bar{E}=0} = -\hat{n} \times \bar{E}_1 \qquad (2.4)$$

This particular form of surface equivalence principle is called as Love's equivalence theorem. Since Love's equivalence theorem creates zero fields inside of closed surface, volume inside of that closed surface can be filled with any material. If it is filled with a Perfect Electrical Conductor (PEC) then the electrical current density over the closed surface will not produce any fields outside of the closed surface so it will be omitted. Same method can be done with Perfect Magnetic Conductor (PMC) material. If it is assumed that the volume inside of the closed surface will be filled with PMC then magnetic current density over the closed surface will not produce any field outside of closed surface, again it is omitted. However, the remaining equivalent current densities will radiate in the presence of the PEC or PMC used to eliminate one of the equivalent currents.
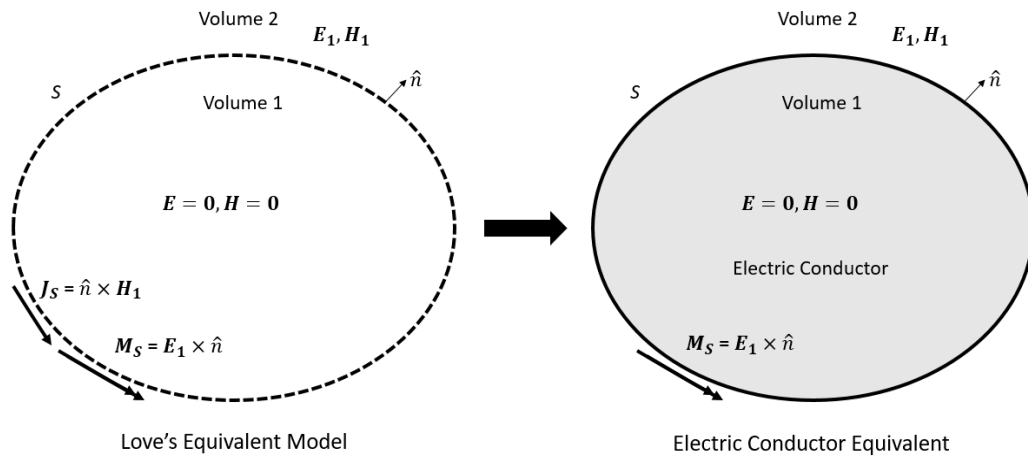
Figure 2.2 Transformation to Electric Conductor Equivalent
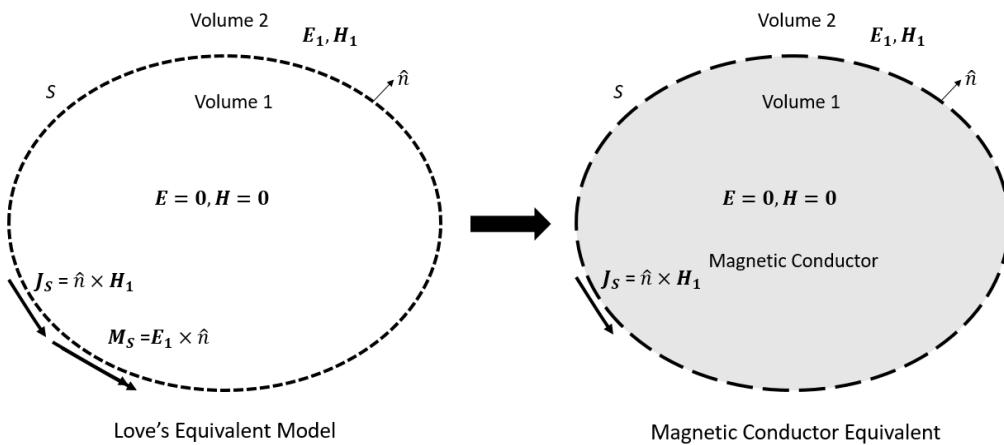
Figure 2.3 Transformation to Magnetic Conductor Equivalent

If the geometry of the conductor permits (i.e. an infinite plane), image theory can be utilized to eliminate the conductor.

Once the equivalent currents are defined over the closed surface, fields outside of that closed surface can be found using vector potentials. Solution in terms of vector potentials will be summarized by starting with Maxwell's equations in phasor domain for a linear, homogeneous, isotropic medium:

$$\nabla \times \bar{E} = -j\omega\mu\bar{H} \tag{2.5}$$

$$\nabla \times \bar{H} = j\omega\mu\varepsilon\bar{E} + \bar{J} \tag{2.6}$$

$$\nabla . \bar{D} = \rho_v \tag{2.7}$$

$$\nabla . \bar{B} = 0 \tag{2.8}$$

Using the null identity $\nabla . (\nabla \times \bar{\varphi}) = 0$ vector potential $\bar{A}$ can be defined as:

$$\nabla \times \bar{A} = \bar{B} = \mu\bar{H} \tag{2.9}$$

By taking the curl of (2.6), expression can be rewritten as:

$$\nabla \times \nabla \times \bar{A} = j\omega\mu\varepsilon\bar{E} + \mu\bar{J} \tag{2.10}$$

Using the vector identity $\nabla \times (\nabla \times \bar{\varphi}) = \nabla(\nabla . \bar{\varphi}) - \nabla^2\bar{\varphi}$ (2.10) can be expressed as:

$$\nabla(\nabla . \bar{A}) - \nabla^2\bar{A} = j\omega\mu\varepsilon\bar{E} + \mu\bar{J} \tag{2.11}$$

Using another null identity $\nabla \times (\nabla N) = 0$ where N is an arbitrary scalar field and (2.5) electric scalar potential (V) can be defined,

$$\bar{E} + j\omega\bar{A} = -\nabla V \tag{2.12}$$

By substituting (2.12) into (2.10),

$$\nabla(\nabla . \bar{A}) - \nabla^2\bar{A} = \omega^2\mu\varepsilon\bar{A} - j\omega\mu\varepsilon\nabla V + \mu\bar{J} \tag{2.13}$$

Rearranging the equation above,

$$\nabla(\nabla . \bar{A} + j\omega\mu\varepsilon V) - \nabla^2\bar{A} = \omega^2\mu\varepsilon\bar{A} + \mu\bar{J} \tag{2.14}$$

Lorentz gauge can be used to simplify the equation where divergence of $\bar{A}$ is selected such that expression inside gradient operator is equal to zero.

$$\nabla . \bar{A} + j\omega\mu\varepsilon\varphi = 0 \tag{2.15}$$

Finally, equation can be written as:

$$\nabla^2\bar{A} + \omega^2\mu\varepsilon\bar{A} = -\mu\bar{J} \tag{2.16}$$

This partial differential equation has a particular solution [18]:

$$\bar{A}(\bar{r}) = \frac{\mu}{4\pi} \int_V \frac{\bar{J}(\bar{r}')e^{-jk|\bar{r}-\bar{r}'|}}{|\bar{r} - \bar{r}'|} dV' \tag{2.17}$$

Where $\bar{r}'$ denotes the position of source and $\bar{r}$ denotes the position of observation point. If the electric current densities are known, magnetic vector potential can be found anywhere which can be used to calculate the fields created by electrical sources.by using following relations [19]:

$$\bar{E} = -j\omega\bar{A} - j\frac{1}{\omega\mu\varepsilon}\nabla(\nabla.\bar{A}) \qquad (2.18)$$

$$\bar{H} = \frac{1}{\mu}\nabla \times \bar{A} \qquad (2.19)$$

An isolated antenna will be simulated by using CST Microwave Studio and tangential field components over a closed surface will be exported. Hence the equivalent current density over the surface is available only at some discrete grid points. Therefore, to calculate the fields radiated by these currents, small dipole approximation [20] is used and the electric field and magnetic field due to a single dipole at origin is expressed as in (2.20) and (2.21).

To find electric field and magnetic field caused by a dipole that is not located at origin, $\bar{r}$ is replaced with $\bar{r} - \bar{r}'$

$$\bar{E}_e(\bar{r}) = \frac{\eta}{4\pi r}\left[\left(\frac{(\bar{r} \cdot \bar{m}_e)\bar{r}}{r^2} - \bar{m}_e\right)P + 2\left(\frac{(\bar{r} \cdot \bar{m}_e)\bar{r}}{r^2}\right)U\right]e^{-jkr} \qquad (2.20)$$

$$\bar{H}_e(\bar{r}) = \frac{jk}{4\pi r^2}(\bar{m}_e \times \bar{r})\left[1 + \frac{1}{jkr}\right]e^{-jkr} \qquad (2.21)$$

$$P = \left(\frac{jk}{r} + U\right) \qquad (2.22)$$

$$U = \left(\frac{1}{r^2} + \frac{1}{jkr^3}\right) \qquad (2.23)$$

Where $\bar{m}_e$ is the electric dipole moment, defined as the product of effective dipole current and effective dipole length. Effective dipole current is the product of equivalent current density at the grid point multiplied by the grid spacing in the transverse direction to the current. Dipole length is the grid spacing along the current direction. Superposition of fields created by each dipole located over closed surface will give the fields created by the transmitter antenna at a certain observation point.

Using this method, it will be possible to find incident field over the scatterer and fields directly coupled to receiver antenna from transmitter antenna. In addition to that, as long as antenna type is same, there is no need to run a full-wave simulation one more time when the transmitter position is changed. Since only the position of the dipole moments will change but their magnitude and direction will remain same.

Magnetic dipoles can be also defined over the closed surface. Using the duality theorem and equations (2.20) and (2.21), fields created by a magnetic dipole at origin at an arbitrary observation point can be defined in equation (2.24) and (2.25). Again, $\bar{r}$ must be replaced with $\bar{r} - \bar{r}'$ and r if dipole is not located at origin.

$$\bar{E}_m(\bar{r}) = -\frac{jk}{4\pi r^2}(\bar{m}_m \times \bar{r})\left[1 + \frac{1}{jkr}\right]e^{-jkr} \tag{2.24}$$

$$\bar{H}_m(\bar{r}) = \frac{1}{4\pi\eta r}\left[\left(\frac{(\bar{r} \cdot \bar{m}_m)\bar{r}}{r^2} - \bar{m}_m\right)P + 2\left(\frac{(\bar{r} \cdot \bar{m}_m)\bar{r}}{r^2}\right)U\right]e^{-jkr} \tag{2.25}$$

Main reason to use small dipole approximation to compute the fields is that, its formulation is valid both for near-field and far-field regions. Accuracy in near-field is especially important to find direct coupling between the antennas in the MIMO system.

To apply surface equivalence theorem any surface shape can be chosen as long as it encloses the antenna. Full-wave simulations are utilized to find the fields over the enclosing surface. In this work CST Microwave Studio is used as full-wave simulator, related data is exported from the simulator. Since CST Microwave Studio only provides an option to export the electromagnetic fields over a rectangular surface, the shape of the enclosed surface must be chosen as a rectangular prism. Normally, six rectangular surfaces should be defined to enclose the antenna. However, in MIMO applications, antennas in the systems are mostly directive. Hence, the fields that are located at the back of the antenna is not included in the calculations since they will be negligibly small compared to radiation in other directions. Neglecting those fields will introduce very small errors but will improve simulation time about twenty percent. Once the fields are exported over the surface, using the surface equivalence theorem, equivalent current densities can be

calculated. Since, fields are exported over a surface, simulator asks user to input a value for spacing interval of the export operation. As this value gets smaller, number of samples that are extracted from the simulator increases. Since this interval is also used to determine dipole moment for each sample point, it has an effect over accuracy. But as expected small intervals causes more samples which increases the calculation time. As a rule of thumb, sampling interval is chosen in such a way that, there are at least twenty samples per wavelength.

To verify the method through numerical examples, as shown in Figure 2.4 a linearly polarized in (x-direction) probe fed circular patch antenna which operates approximately around 1.5 GHz is designed.
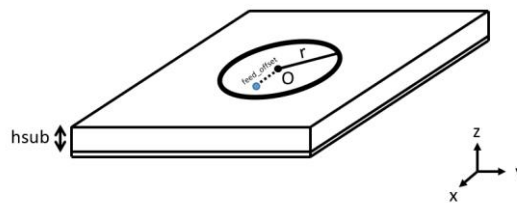

Figure 2.4 Structure of Patch Antenna

 Diameter of the circular patch is 60.3 mm, whereas the feed offset from the center is equal to 6.55 mm. Rogers RO4003C material is used as a dielectric substrate which has dielectric constant of 3.55 and its loss tangent is equal to 0.0027. Substrate thickness is chosen as 1.524 mm.

Input return loss, 3D radiation pattern, E-plane and H-plane radiation patterns at 1.5 GHz obtained by CST simulations are presented in Figure 2.5, Figure 2.6, Figure 2.7 and Figure 2.8, respectively.
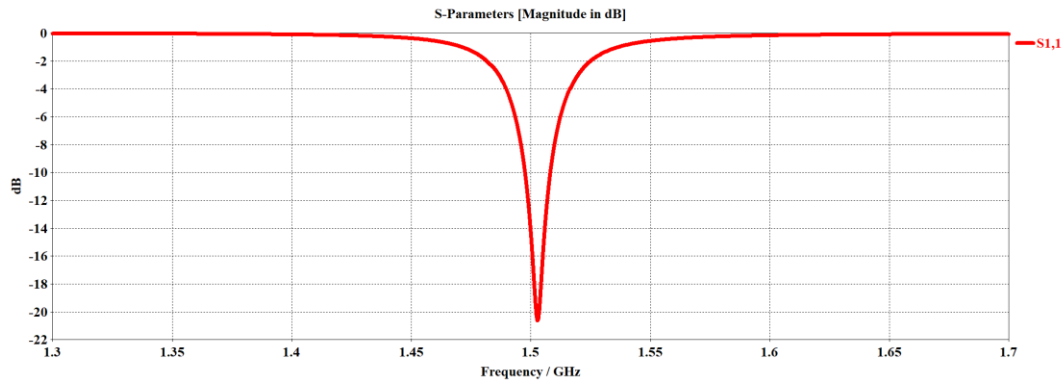
Figure 2.5 Return Loss (S11) of the patch antenna with respect to frequency
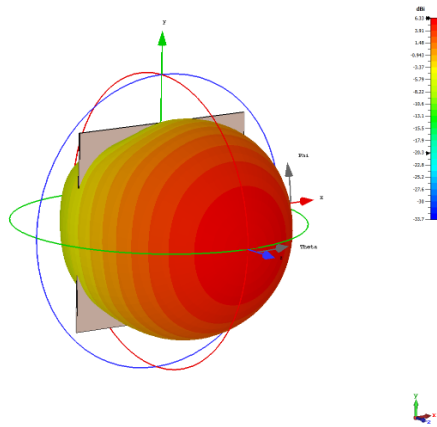

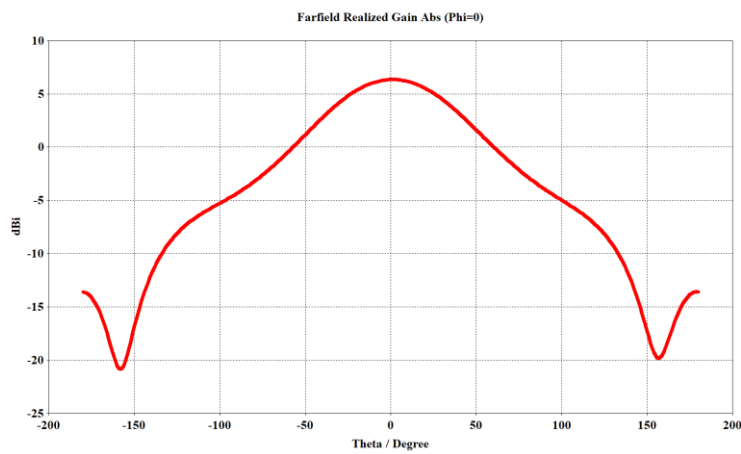Figure 2.6 3D Radiation Pattern of Patch Antenna (1.5 GHz)

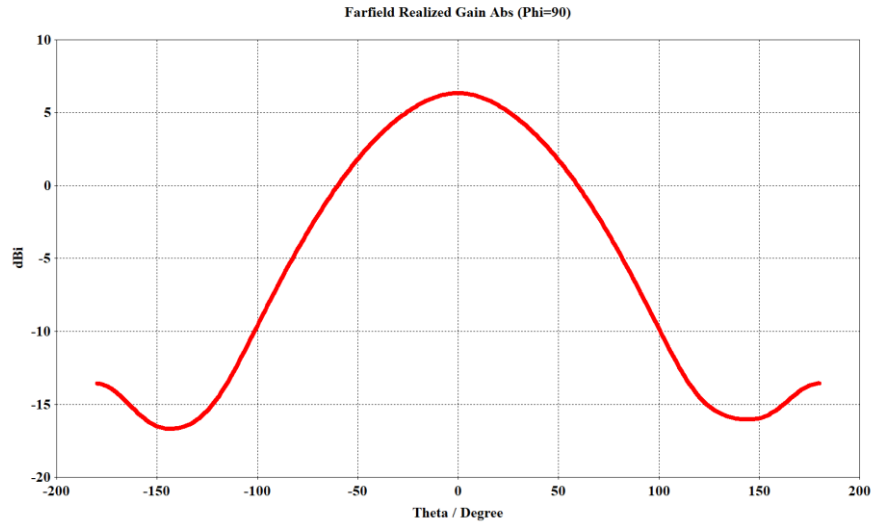Figure 2.7 E-plane Radiation Pattern of Patch Antenna (1.5 GHz)

Figure 2.8 H-plane Radiation Pattern of Patch Antenna (1.5 GHz)

With an effort to decrease simulation time first, only fields at the front surface of the enclosing surface are used to compute the fields over a square plane that is 450mm farther away from the antenna as shown in Figure 2.9. At the same time, fields over that observation plane are also extracted from CST Microwave Studio and results are compared with each other.

Results of CST and radiated field calculation by small dipole approximation method are compared for three different dimensions of front surface: ($[\lambda \times \lambda]$ and $[1.5\lambda \times 1.5\lambda]$) to see the effect of size of front surface. Surface is chosen as 10 mm away from the antenna and sampling interval of exported data is chosen as 10 mm in both directions. Results are presented only for dominant components of electric field and magnetic field. Since antenna is horizontally polarized, X-component of E-field and Y-component of H-field are dominant components.
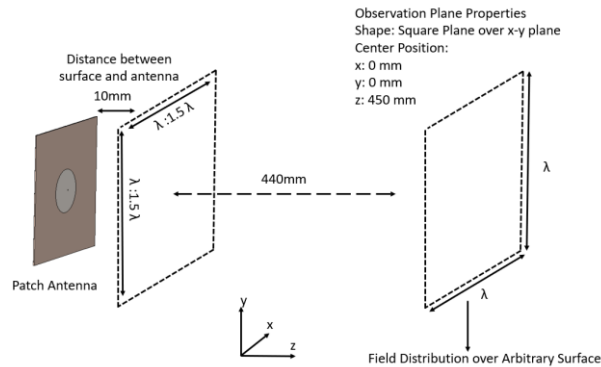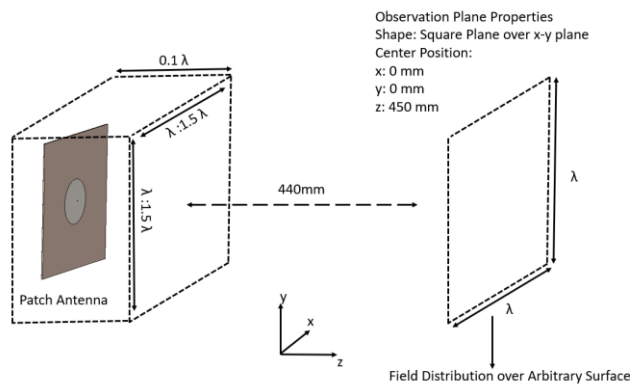
15

Figure 2.9: Simulation Scenario (1 surface)

Figure 2.10: Simulation Scenario (5 surfaces)

The magnitude and phase of electric field is compared with the results of CST for two different box sizes in Figure 2.11 and Figure 2.12, respectively. The left column is for front surface size of $\lambda \times \lambda$ and right column is for front surface size of $1.5\lambda \times 1.5\lambda$. The first row is for field calculation only by using the front surface, the second row is for the calculation by using 5 surfaces. The third row shows CST results. To better interpret the level of error, for each case the percentage error in magnitude with respect to results of CST is plotted in Figure 2.13, whereas the absolute phase error distribution is presented in Figure 2.14. Similarly, magnitude and phase distributions of magnetic field intensity are given in Figure 2.15 and Figure 2.16, respectively. The percentage error in magnitude and phase error for magnetic field are compared in Figure 2.17 and Figure 2.18, respectively. Finally, mean values of

16

errors in magnitudes and phases of electric and magnetic fields are summarized in Table 2.1.

By investigating the results, it can be observed that when using only front surface error decreases considerably by increasing the size of the surface. Similarly, when 4 side surfaces are included into the calculations in addition to the front surface, the accuracy of $\lambda \times \lambda$ sized front surface case increases as expected. However, same improvement in accuracy cannot be observed for $1.5\lambda \times 1.5\lambda$ sized front surface case. This may be due to the fact that we may be at the limits of the best accuracy we can achieve through small dipole approximation for a discretization with step size of 10mm ($\lambda/20$). Changing the box size and adding more faces may be resulting in marginal changes around this accuracy level and causing unexpected fluctuations. If a better accuracy is desired, the step size in discretization should be decreases. However, this results in longer computation times and larger memory requirement. As it will be demonstrated at the end of Chapter 4, due to the variational nature of reaction integrals, the error in field distributions contributes less to the mutual impedance results calculated by these fields.
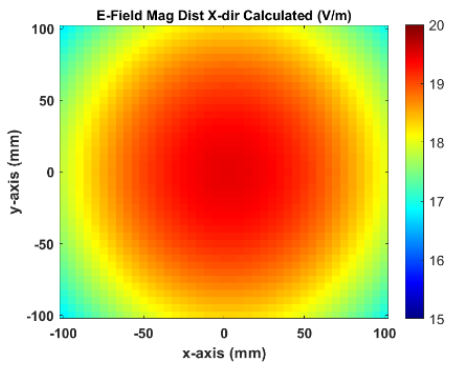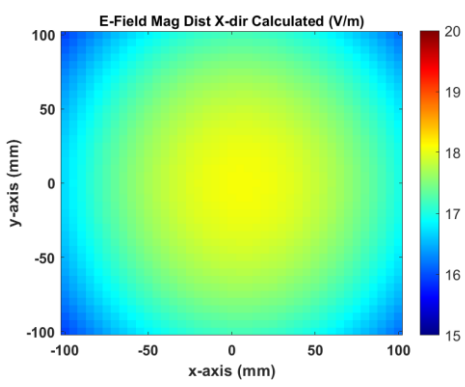
λ × λ front surface   **1.5λ × 1.5λ front surface**

(a) only front surface   (b) only front surface
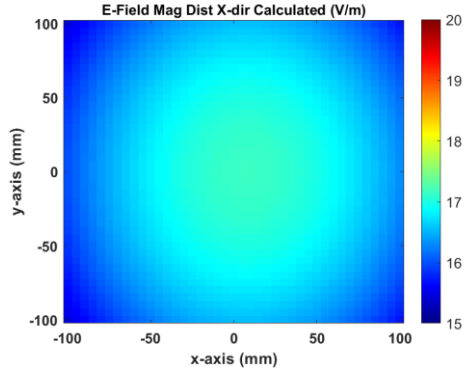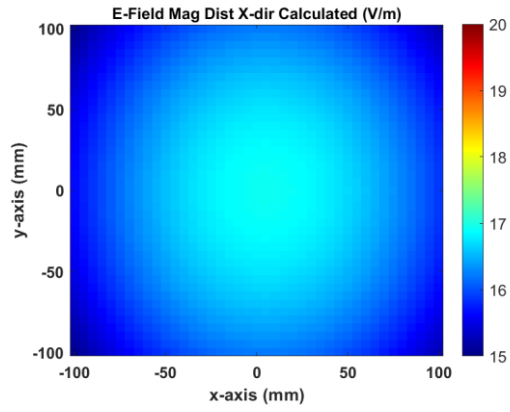
(c) 5 surfaces   (d) 5 surfaces

(e) CST

Figure 2.11: Magnitude Distribution Comparison of E-field

18

λ × λ front surface   **1.5λ × 1.5λ front surface**

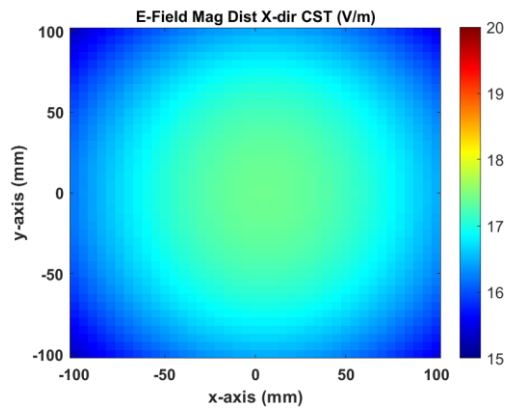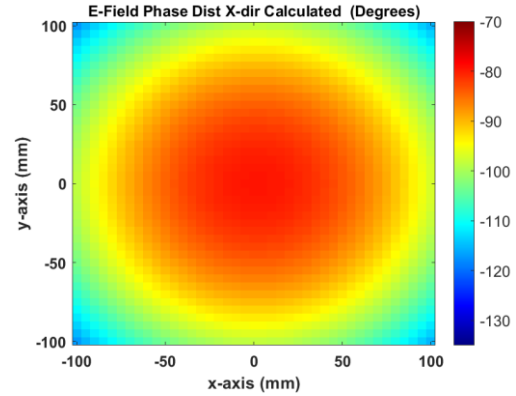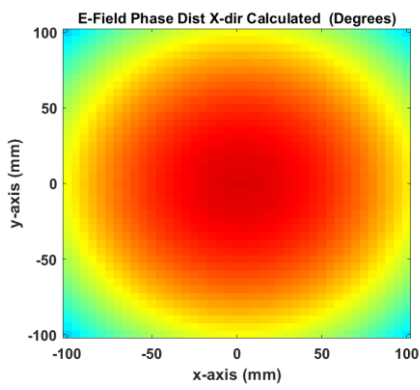(a) only front surface   (b) only front surface
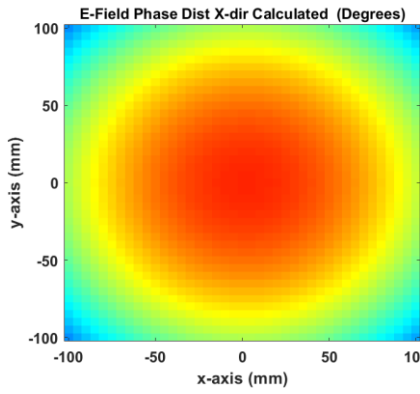
(c) 5 surfaces   (d) 5 surfaces

(e) CST

Figure 2.12: Phase Distribution Comparison of E-field
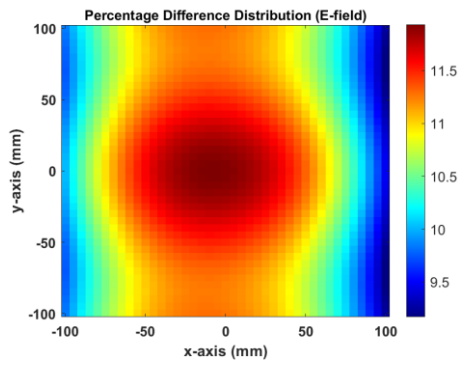
λ × λ front surface   **1.5λ × 1.5λ front surface**

(a) only front surface
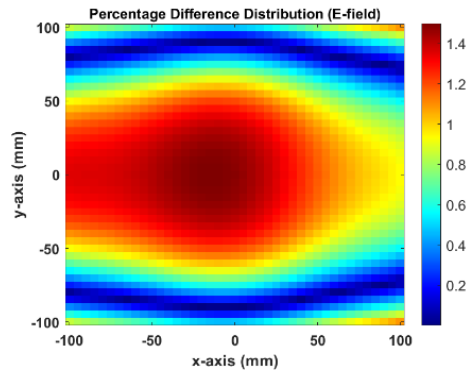
(b) only front surface

(c) 5 surfaces

(d) 5 surfaces

Figure 2.13: Percentage Difference Distribution of E-field
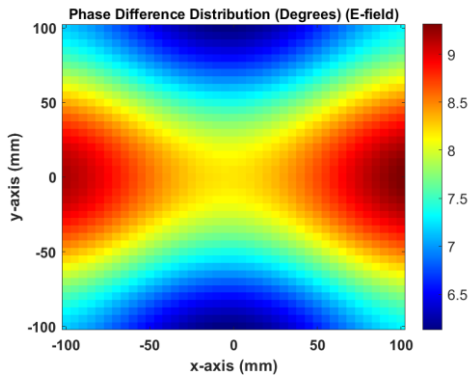
λ × λ front surface   **1.5λ × 1.5λ front surface**

(a) only front surface   (b) only front surface
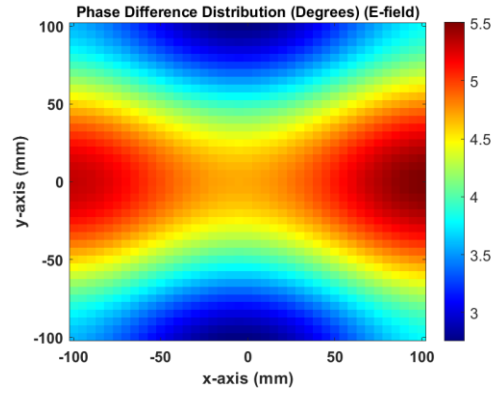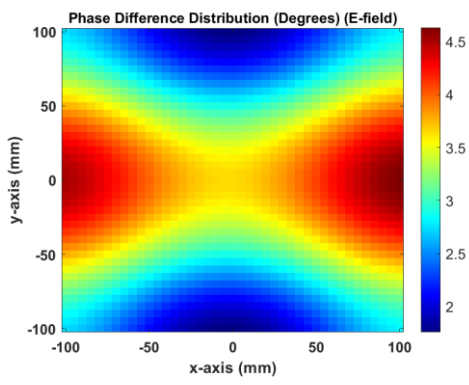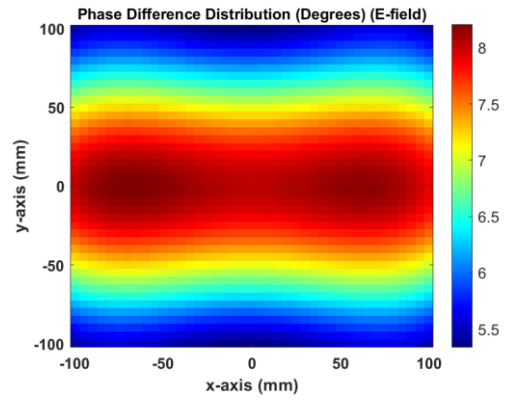
(c) 5 surfaces   (d) 5 surfaces

Figure 2.14: Phase Difference Distribution of E-field
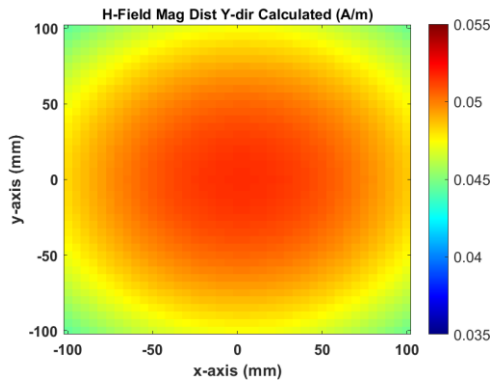
λ × λ front surface　　　　　　　**1.5λ × 1.5λ front surface**

(a) only front surface　　　　　　(b) only front surface
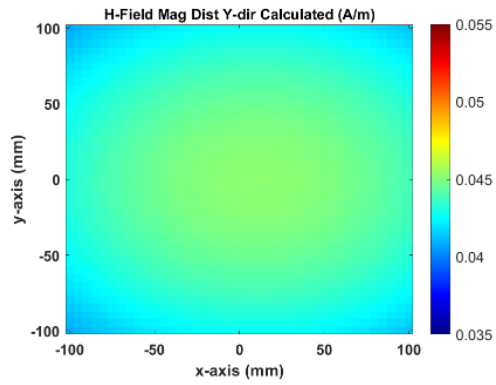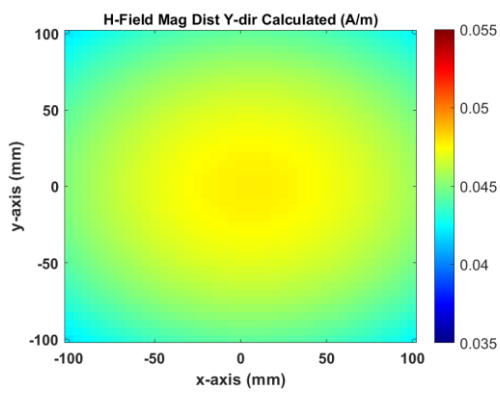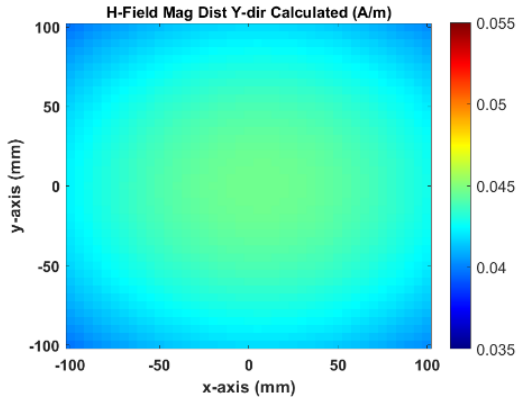
(c) 5 surfaces　　　　　　　　　(d) 5 surfaces
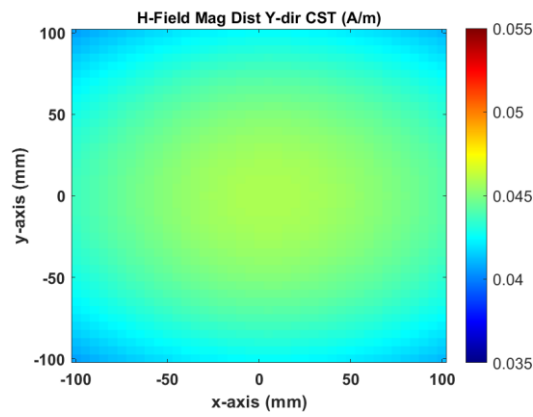
(e) CST

Figure 2.15: Magnitude Distribution Comparison of H-field
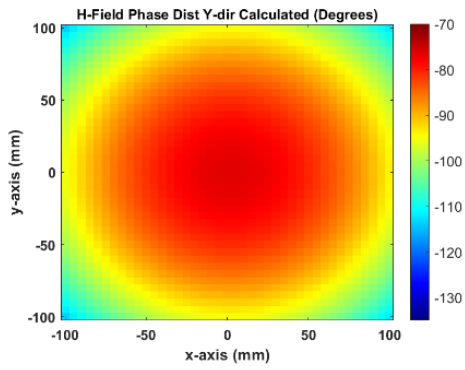
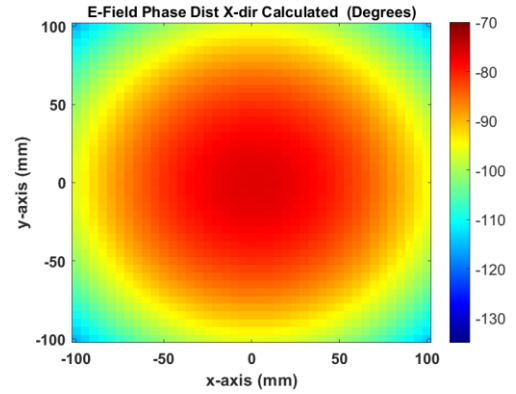**λ × λ front surface** **1.5λ × 1.5λ front surface**
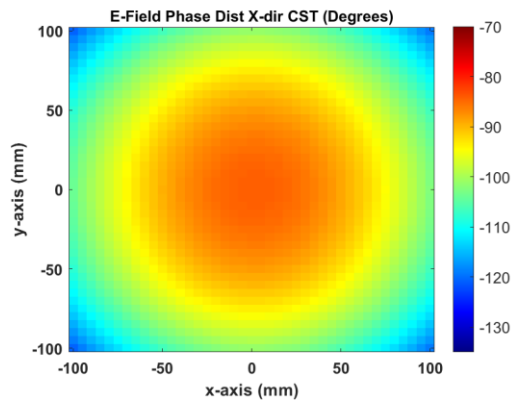

(a) only front surface (b) only front surface
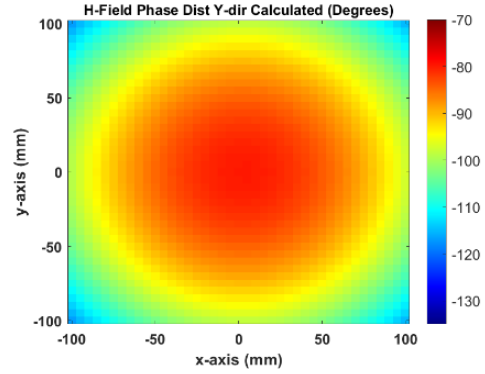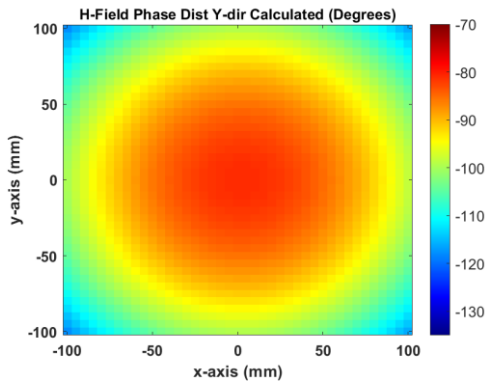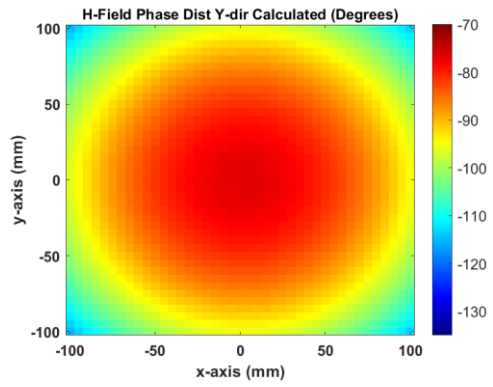
(c) 5 surfaces (d) 5 surfaces
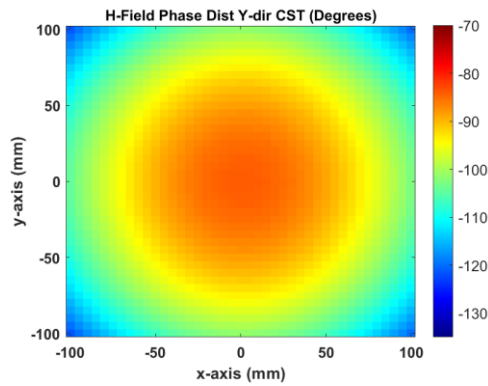
(e) CST

Figure 2.16: Phase Distribution Comparison of H-field
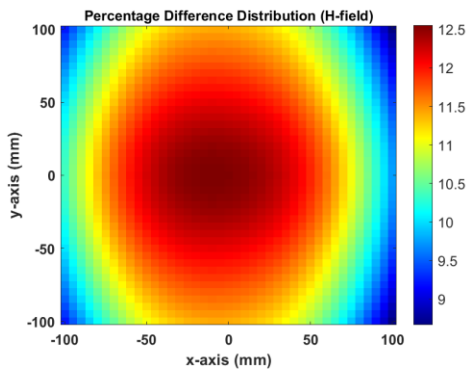
λ × λ front surface **1.5λ × 1.5λ front surface**

(a) only front surface
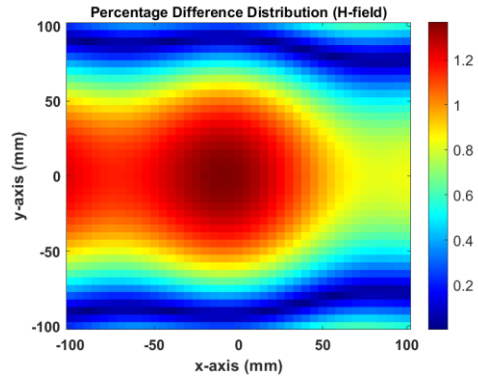
(b) only front surface
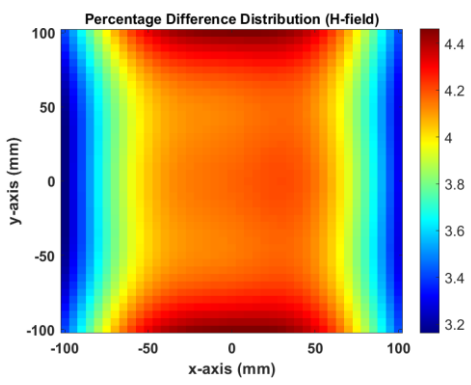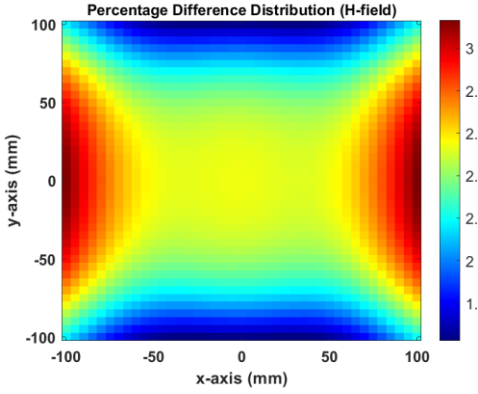
(c) 5 surfaces

(d) 5 surfaces

Figure 2.17: Percentage Difference Distribution of H-field
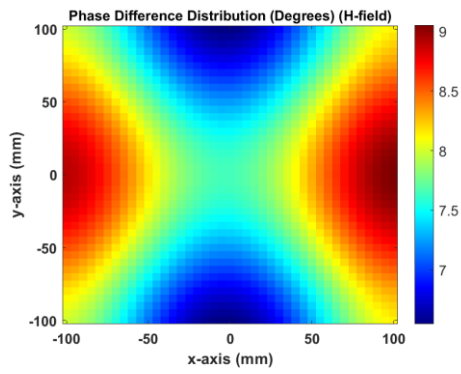
24

λ × λ front surface　　　　　**1.5λ × 1.5λ front surface**

(a) only front surface　　　　　(b) only front surface
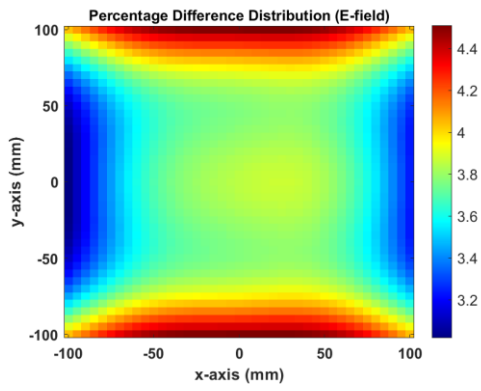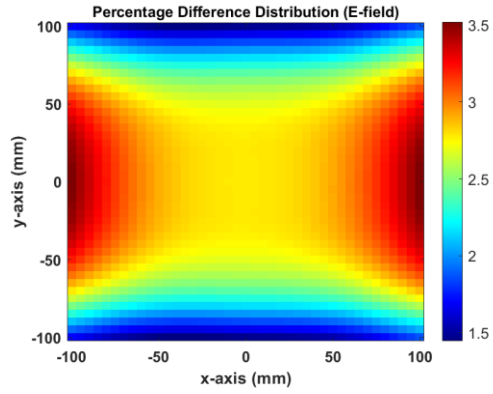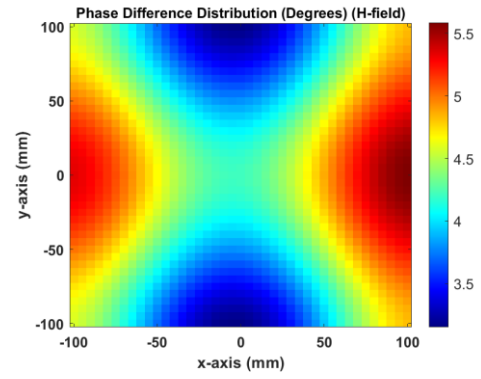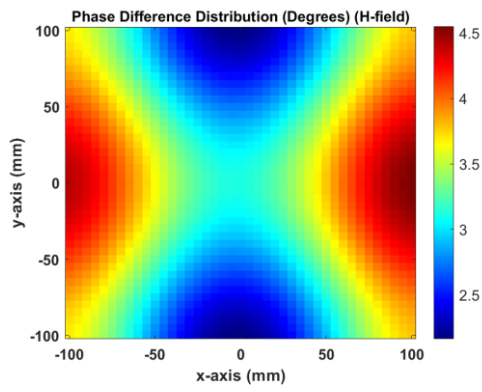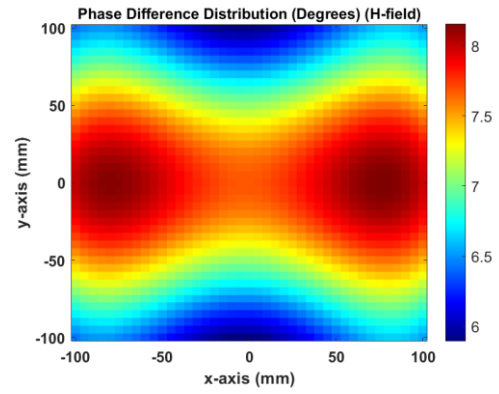

(c) 5 surfaces　　　　　(d) 5 surfaces

Figure 2.18: Phase Difference Distribution of H-field

Error Type / Surface Type	Mean Error in Magnitude (Percentage)		Mean Error in Phase (Degrees)	
	E-field	H-field	E-field	H-field
$[\lambda \times \lambda]$ 1 Surface	10.88	11.17	7.77	7.85
$[1.5\lambda \times 1.5\lambda]$ 1 Surface	0.86	0.70	4.19	4.38
$[\lambda \times \lambda]$ 5 surfaces	3.77	3.97	3.23	3.37
$[1.5\lambda \times 1.5\lambda]$ 5 surfaces	2.62	2.39	6.98	7.25

Table 2.1: Error Comparison Table for Different Surface Types

CHAPTER 3

APPLICATION OF METHOD OF MOMENTS

In this chapter, application of Method of Moments (MoM) technique will be explained to find the surface currents induced over the scatterer due to the fields radiated by the transmitter antenna. Electric field integral equations (EFIE) will be employed to find the induced currents since there is already a well-developed procedure for this kind of calculations. Also, unlike magnetic field integral equations (MFIE), EFIE can be easily applied to open surfaces as well so it is more appropriate for different target shapes. [21]

Scattered electric field due to induced electric current density $\bar{J}$ can be found with the following equation:

$$\bar{E}^s = -j\omega\bar{A} - \nabla\varphi \tag{3.1}$$

where magnetic vector potential $\bar{A}$ can be written as,

$$\bar{A}(\bar{r}) = \frac{\mu}{4\pi} \int\limits_S \frac{\bar{J}(\bar{r}')e^{-jk|\bar{r}-\bar{r}'|}}{|\bar{r} - \bar{r}'|} dS' \tag{3.2}$$

and electric scalar potential φ can be written as:

$$\varphi(\bar{r}) = \frac{1}{4\pi\varepsilon} \int\limits_S \rho \frac{e^{-jk|\bar{r}-\bar{r}'|}}{|\bar{r} - \bar{r}'|} dS' \tag{3.3}$$

Charge density ρ is related to current density through the following continuity equation

$$\nabla.\bar{J} = -j\omega\rho \tag{3.4}$$

The tangential component of the total electric field should be zero over the surface of the PEC scatterer. This boundary condition can be written in terms of incident $\bar{E}^i$ and scattered fields $\bar{E}^s$

$$\hat{n} \times \left(\bar{E}^i + \bar{E}^s \right) = 0 \qquad (3.5)$$

Then integro-differential equation can be constructed as:

$$-\bar{E}_{tan}^i = \left(-\frac{j\omega\mu}{4\pi} \int_S \frac{\bar{J}(\bar{r}')e^{-jk|\bar{r}-\bar{r}'|}}{|\bar{r}-\bar{r}'|} dS' + \nabla \frac{1}{j\omega 4\pi\varepsilon} \int_S \nabla \cdot \bar{J} \frac{e^{-jk|\bar{r}-\bar{r}'|}}{|\bar{r}-\bar{r}'|} dS' \right)_{tan} \qquad (3.6)$$

Rao-Wilton-Glisson (RWG) basis functions defined below [22] are used to expand the induced current.:

$$\bar{f}_n(\bar{r}) = \begin{cases} \dfrac{l_n}{2A_n^+} \bar{\rho}_n^+, & \bar{r} \text{ in } T_n^+ \\ \dfrac{l_n}{2A_n^-} \bar{\rho}_n^-, & \bar{r} \text{ in } T_n^- \\ 0, & otherwise, \end{cases} \qquad (3.7)$$

Where l_n is the length of nth edge element, $A_n^{\mp}$ is the area of triangle $T_n^{\mp}$ and $\bar{\rho}_n^+$ is the vector that goes from free vertex of the triangle T_n^+ to an arbitrary point inside of the corresponding triangle. As shown in Figure 3.1 on the other hand, $\bar{\rho}_n^-$ denotes the vector that starts from an arbitrary point in T_n^- triangle and ends at free vertex of that triangle.
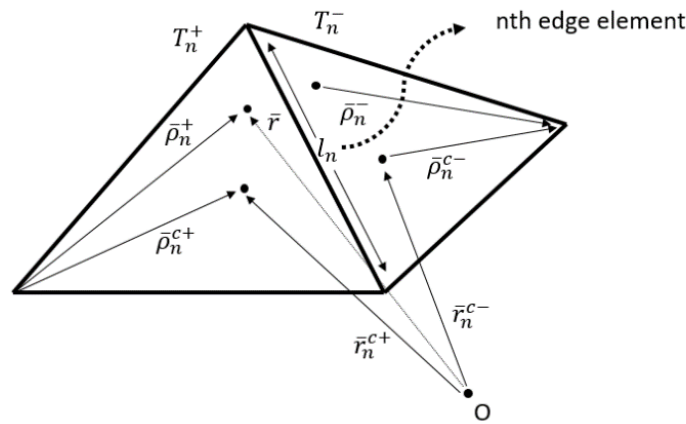
Figure 3.1: Triangle pair shown for n^{th} edge element

Divergence of the basis function is defined as,

$$\nabla \cdot \bar{f}_n = \begin{cases} \dfrac{l_n}{A_n^+}, & \bar{r} \; in \; T_n^+ \\ -\dfrac{l_n}{A_n^-}, & \bar{r} \; in \; T_n^- \\ 0, & otherwise, \end{cases} \tag{3.8}$$

Current density over the surface is approximated as:

$$\bar{J} = \sum_{n=1}^{N} I_n \bar{f}_n(\bar{r}) \tag{3.9}$$

Where N denotes the total number of non-boundary edge in the surface. Main objective here is to find coefficients of basis functions for each edge element which is denoted by I_n.

Galerkin approach is used so testing and basis functions are chosen to be same. By substituting (3.9) into (3.6) and testing equation (3.6) with RWG functions, following N equations are obtained for each m value:

$$\langle \bar{E}^i, \bar{f}_m \rangle = j\omega\langle \bar{A}, \bar{f}_m \rangle + \langle \nabla\varphi, \bar{f}_m \rangle \; for \; m = 1, 2, \dots N \tag{3.10}$$

The gradient operator acting on φ in the second term of right-hand side can be transferred onto $\bar{f}_m$ by using integration by parts.

$$\langle \nabla\varphi, \bar{f}_m \rangle = -\int_S \varphi \nabla_s \cdot \bar{f}_m \, dS \tag{3.11}$$

By substituting (3.8) into (3.11) it takes the following form:

$$\int_S \varphi \nabla_s \cdot \bar{f}_m \, dS = l_m \left(\frac{1}{A_m^+} \int_{T_m^+} \varphi dS - \frac{1}{A_m^-} \int_{T_m^-} \varphi dS \right) \tag{3.12}$$

The integral expressions on the right-hand side can be approximated as the product of the area of the triangle and the value of φ at the center point of that triangle. Therefore, right-hand side can be rewritten as:

$$\int_S \varphi \nabla \cdot \bar{f}_m \, dS \approx l_m [\varphi(\bar{r}_m^{c+}) - \varphi(\bar{r}_m^{c-})] \tag{3.13}$$

where $\bar{r}_m^{c+}$ and $\bar{r}_m^{c-}$ are position vectors to the centers of T_m^+ and T_m^- triangles, respectively. The same approximation is applied for the testing integrals of the incident field and the vector potential terms given in (3.11). As a result, following relations are obtained:

$$\left\langle \begin{Bmatrix} \bar{E}^i \\ \bar{A} \end{Bmatrix}, \bar{f}_m \right\rangle = l_m \left[\frac{1}{2A_m^+} \int_{T_m^+} \begin{Bmatrix} \bar{E}^i \\ \bar{A} \end{Bmatrix} \cdot \bar{\rho}_m^+ \, dS + \frac{1}{2A_m^-} \int_{T_m^-} \begin{Bmatrix} \bar{E}^i \\ \bar{A} \end{Bmatrix} \cdot \bar{\rho}_m^- \, dS \right]$$

$$\approx \frac{l_m}{2} \left[\begin{Bmatrix} \bar{E}^i(\bar{r}_m^{c+}) \\ \bar{A}(\bar{r}_m^{c+}) \end{Bmatrix} \cdot \bar{\rho}_m^{c+} + \begin{Bmatrix} \bar{E}^i(\bar{r}_m^{c-}) \\ \bar{A}(\bar{r}_m^{c-}) \end{Bmatrix} \cdot \bar{\rho}_m^{c-} \right] \tag{3.14}$$

Where $\bar{\rho}_m^{c-}$ vector denotes the vector that starts from the center of triangle T_m^- and ends at free vertex of that triangle. However, $\bar{\rho}_m^{c+}$ vector starts from free vertex of triangle T_m^+ and ends at the center of that triangle.

These N equations can be written in matrix from as follows:

$$[Z][I] = [V] \tag{3.15}$$

Now all the inner product expressions are defined, integro-differential equation (3.10) can be rewritten as below by using the inner product expressions found in (3.13) and (3.16):

$$\frac{l_m}{2} \left[\bar{E}^i(\bar{r}_m^{c+}) \cdot \bar{\rho}_m^{c+} + \bar{E}^i(\bar{r}_m^{c-}) \cdot \bar{\rho}_m^{c-} \right]$$

$$= j\omega \frac{l_m}{2} [\bar{A}(\bar{r}_m^{c+}) \cdot \bar{\rho}_m^{c+} + \bar{A}(\bar{r}_m^{c-}) \cdot \bar{\rho}_m^{c-}]$$

$$+ l_m [\varphi(\bar{r}_m^{c-}) - \varphi(\bar{r}_m^{c+})] \, for \, m = 1,2, \dots N \tag{3.16}$$

Each entry of the impedance matrix [Z] models the field at the mth testing function due the nth basis function.

It can be written as:

$$Z_{mn} = j\omega \frac{l_m}{2} [\bar{A}_{mn}^+ \cdot \bar{\rho}_m^{c+} + \bar{A}_{mn}^- \cdot \bar{\rho}_m^{c-}] + l_m [\varphi_{mn}^- - \varphi_{mn}^+] \tag{3.17}$$

Where $\bar{A}_{mn}^{\mp}$ and $\varphi_{mn}^{\mp}$ are given in following expressions:

$$\bar{A}_{mn}^{\mp} = \frac{\mu}{4\pi} \left[\frac{l_n}{2A_n^+} \int_{T_n^+} \bar{\rho}_n^+(\bar{r}') \frac{e^{-jk|\bar{r}_m^{c\mp}-\bar{r}'|}}{|\bar{r}_m^{c\mp}-\bar{r}'|} dS' + \frac{l_n}{2A_n^-} \int_{T_n^-} \bar{\rho}_n^-(\bar{r}') \frac{e^{-jk|\bar{r}_m^{c\mp}-\bar{r}'|}}{|\bar{r}_m^{c\mp}-\bar{r}'|} dS' \right] \quad (3.18)$$

$$\varphi_{mn}^{\mp} = -\frac{1}{4\pi j\omega\varepsilon} \left[\frac{l_n}{A_n^+} \int_{T_n^+} \frac{e^{-jk|\bar{r}_m^{c\mp}-\bar{r}'|}}{|\bar{r}_m^{c\mp}-\bar{r}'|} dS' - \frac{l_n}{A_n^-} \int_{T_n^-} \frac{e^{-jk|\bar{r}_m^{c\mp}-\bar{r}'|}}{|\bar{r}_m^{c\mp}-\bar{r}'|} dS' \right] \quad (3.19)$$

Also, entries of voltage excitation vector caused by the incident field over the surface of scatterer can be calculated with the following expression:

$$V_m = \frac{l_m}{2} \left[\bar{E}_m^+ \cdot \bar{\rho}_m^{c+} + \bar{E}_m^- \cdot \bar{\rho}_m^{c-} \right] \quad (3.20)$$

Where,

$$\bar{E}_m^{\mp} = \bar{E}^i(\bar{r}_m^{c\mp}) \quad (3.21)$$

Integrals in (3.18) and (3.19) can be approximated at center points only, using the same approach for inner products in testing procedure. However, this will introduce too much error, especially for diagonal entries.
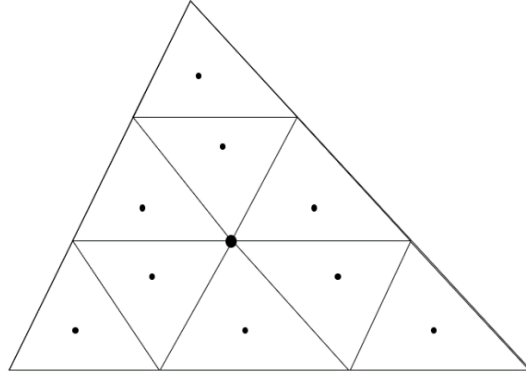

Figure 3.2 Barycentric Subdivision of Triangle Sub-domains

In order to numerically compute those integrals barycentric subdivision [23] method is used. Instead of approximating the integral at the center of the triangle, this approach divides a triangle into sub triangles as shown in Figure 3.2. Each edge of

the triangle is divided to three equal parts, thus creating 9 different sub-triangles. Once the center of each sub-triangle is determined, integral expression is approximated at each center point and calculated as following:

$$\int_{T_n^{\mp}} \frac{e^{-jk|\bar{r}-\bar{r}'|}}{|\bar{r}-\bar{r}'|} dS' = \frac{A_n^{\mp}}{9} \sum_{k=1}^{9} \frac{e^{-jk|\bar{r}-\bar{r}_k^c|}}{|\bar{r}-\bar{r}_k^c|} \qquad (3.22)$$

Note that $A_n^{\mp}$ is denoting the area of the triangle, not the magnetic vector potential.

Voltage excitation vector is affected by the radiation characteristic of the transmitter antenna, meaning that if the transmitter antenna type is changed, all the entries in voltage excitation vector must be recalculated. Whereas, entries in impedance matrix are only affected by the shape and the position of the target, so as long as the position and the shape of the target remains same, impedance matrix entries do not need to be recalculated and. As a result, for different transmitter antennas matrix equation is solved for different right hand side vectors.

Once, current density coefficients for each edge element are found, small dipole approximation can be employed to find scattered electric field and magnetic field created by the target at an arbitrary observation point.

Dipole moment for each edge element can be defined as follows [24]:

$$\bar{m} = \int_{T_n^+ + T_n^-} l_m \bar{f}_m(\bar{r}) dS = l_m I_m (\bar{r}_m^{c-} - \bar{r}_m^{c+}) \qquad (3.23)$$

Where, $l_m I_m$ expression can be interpreted as effective current of the dipole and $(\bar{r}_m^{c-} - \bar{r}_m^{c+})$ contains information about dipole length and direction of current vector. Using equations (2.20) and (2.21) presented in Chapter 2, electromagnetic fields created by each dipole moment can be determined at an observation point. Scattered fields created by the target is equal to the superposition of those fields created by each dipole.

To create triangular meshes for target, a mesh generator called GMSH is used. Program itself has many capabilities, but only 2D mesh generation and geometry

import-export capabilities are required for implementation. GMSH supports .step files as an import option. Since CST Microwave Studio also support export option for .step file, any PEC target that is modeled in CST can be discretized in GMSH platform seamlessly.

Another utility of GMSH mesh generator is that, once the meshing operation is done as shown in Figure 3.3 and Figure 3.4, mesh model can be imported as .stl file which contains information of every triangle corner position and assigns a unique number to each corner so that it will be possible to determine which triangle contains which corner. In addition to that, .stl files are also very easy to export and use in MATLAB, which is the platform that is used for the implementations of the methods explained in this thesis.
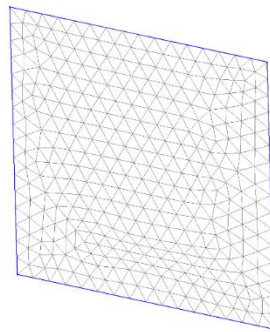

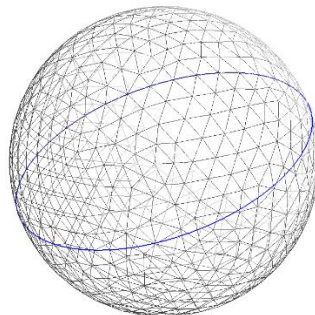Figure 3.3 Plate Target Meshed in GMSH Platform

Figure 3.4 Sphere Target Meshed in GMSH Platform

To test the code developed for implementation of MoM, its results and Mie series [18] results are compared. Since scattered wave from a PEC sphere scatterer is known for a plane wave incidence, MoM solution is constructed for this scenario and they are compared to Mie series results.
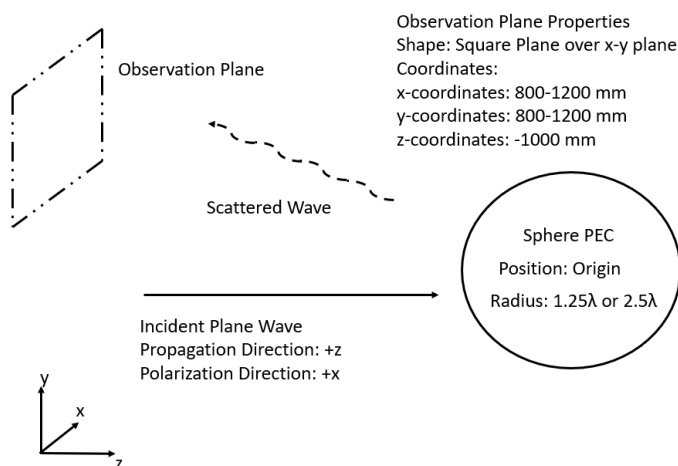

Figure 3.5 Comparison Scenario

Only dominant field components (E_x and H_y) are examined. Magnitude and phase distribution of those fields are given in Figure 3.6 - Figure 3.11 for a PEC sphere that has 2.5λ radius.
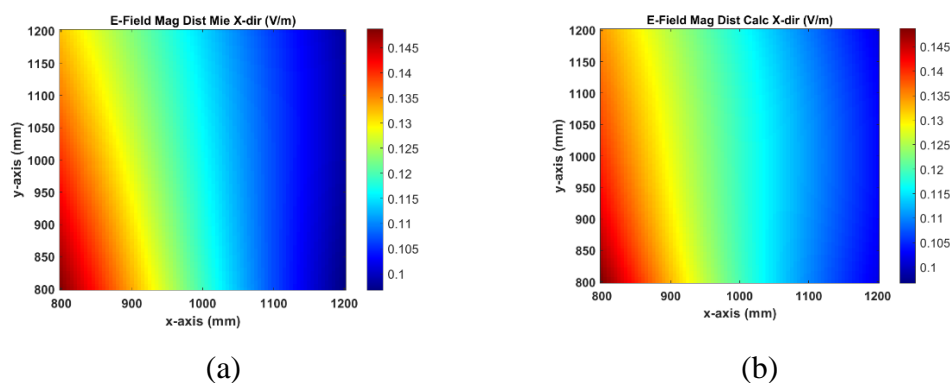

(a)	(b)

Figure 3.6 Magnitude Distribution of Scattered E-Field over Arbitrary Surface (2.5λ Radius Sphere) (a) Mie (b) MoM

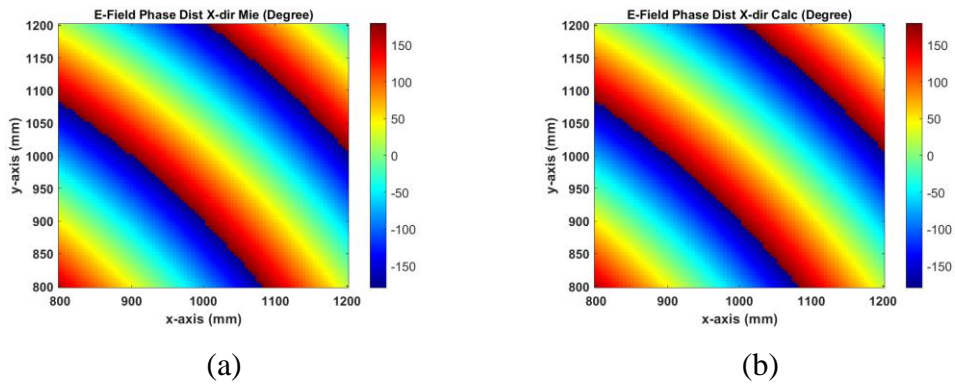(a)   (b)

Figure 3.7 Phase Distribution of Scattered E-Field over Arbitrary Surface (2.5λ Radius Sphere) (a) Mie (b) MoM

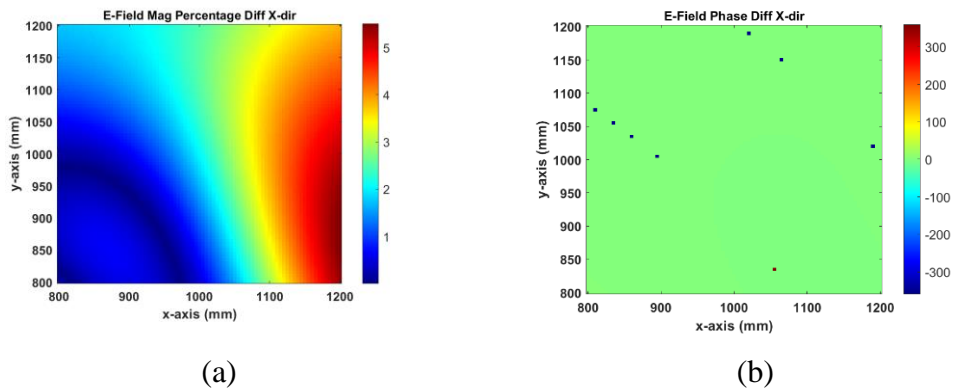(a)   (b)

Figure 3.8 Error Distribution over Surface for E-field (2.5λ Radius Sphere) (a) Magnitude (b) Phase

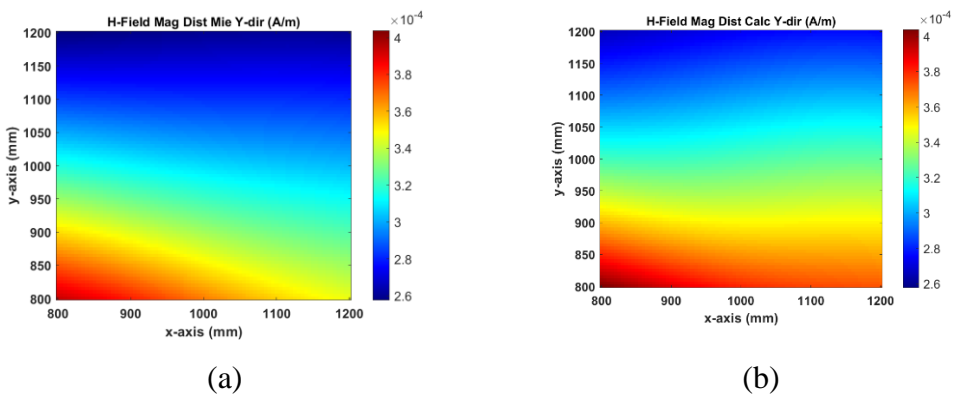(a)   (b)

Figure 3.9 Magnitude Distribution of Scattered H-Field over Arbitrary Surface (2.5λ Radius Sphere) (a) Mie (b) MoM

(a)   (b)
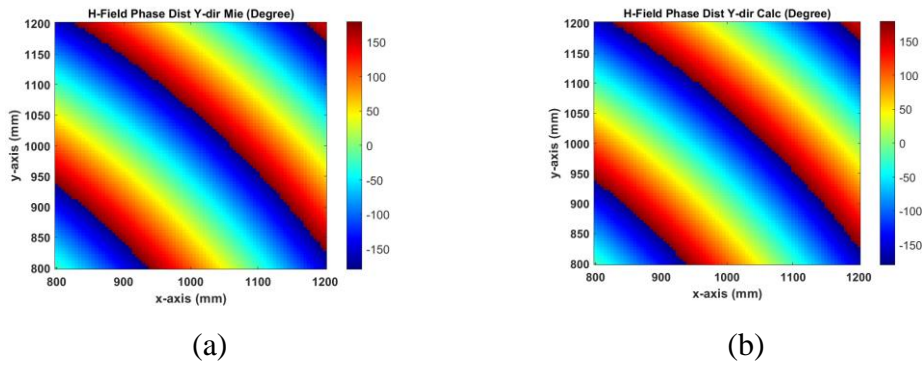
Figure 3.10 Phase Distribution of Scattered H-Field over Arbitrary Surface (2.5λ Radius Sphere) (a) Mie (b) MoM

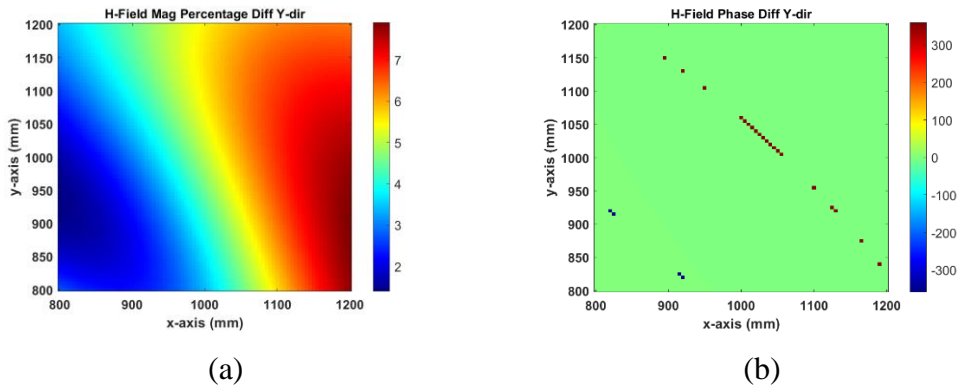(a)   (b)

Figure 3.11 Error Distribution over Surface for H-field (2.5λ Radius Sphere) (a) Magnitude (b) Phase

For a PEC sphere that has 2.5λ radius mean magnitude error for E-field is 2.27 percent and for H-field is equal to 4.79 percent. Mean phase error for E-field is equal to 0.15 degrees. For H-field it is equal to 0.47 degrees.
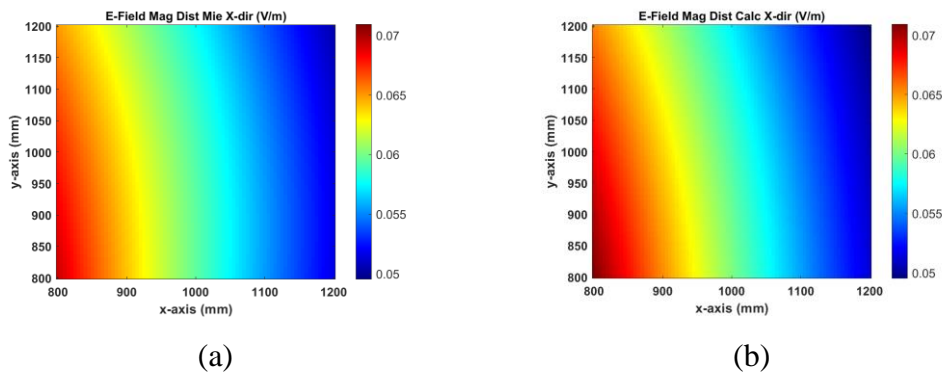

(a)   (b)

Figure 3.12 Magnitude Distribution of Scattered E-Field over Arbitrary Surface (1.25λ Radius Sphere) (a) Mie (b) MoM
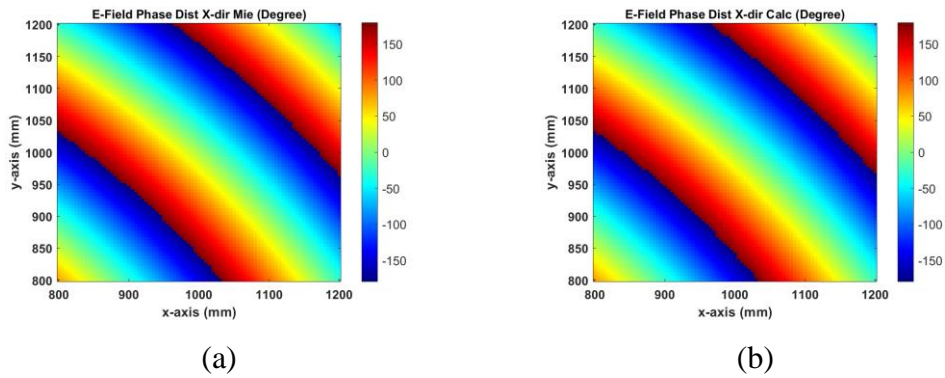
36

(a)   (b)

Figure 3.13 Phase Distribution of Scattered E-Field over Arbitrary Surface (1.25λ Radius Sphere) (a) Mie (b) MoM
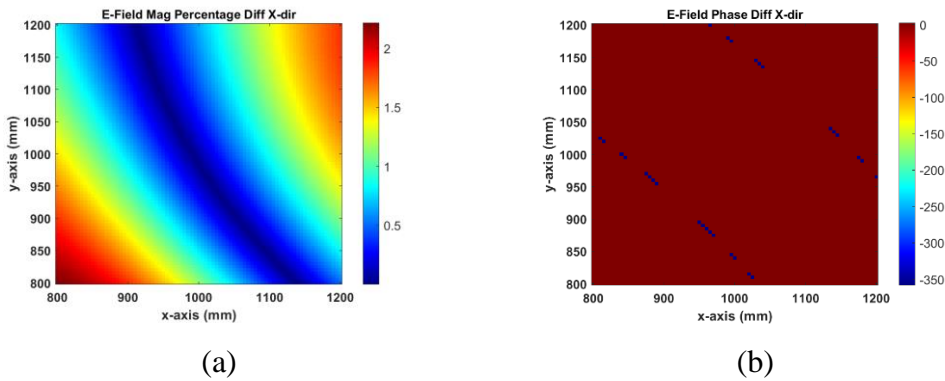

(a)   (b)

Figure 3.14 Error Distribution over Surface for E-field (1.25λ Radius Sphere) (a) Magnitude (b) Phase
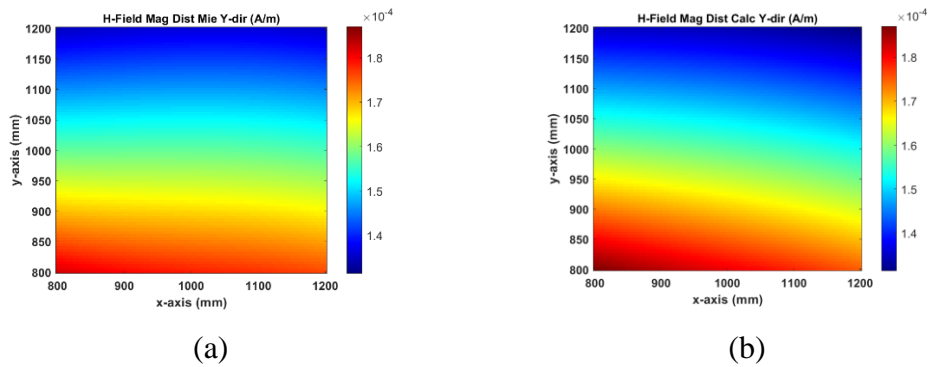

(a)   (b)

Figure 3.15 Magnitude Distribution of Scattered H-Field over Arbitrary Surface (1.25λ Radius Sphere) (a) Mie (b) MoM

(a)   (b)
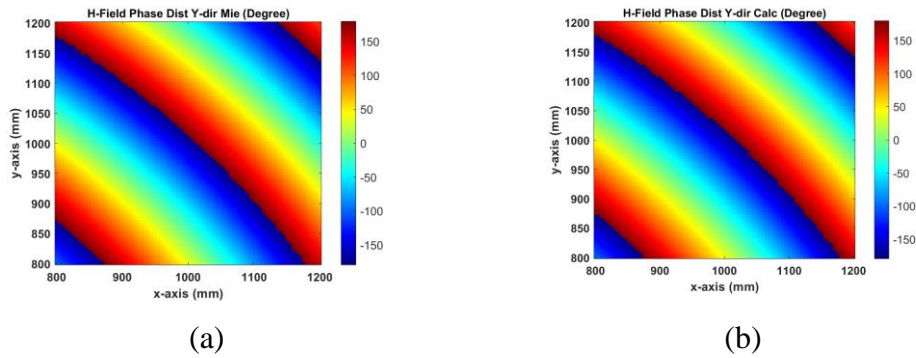
Figure 3.16 Phase Distribution of Scattered H-Field over Arbitrary Surface (1.25λ Radius Sphere) (a) Mie (b) MoM

(a)   (b)

Figure 3.17 Error Distribution over Surface for H-field (1.25λ Radius Sphere) (a) Magnitude (b) Phase
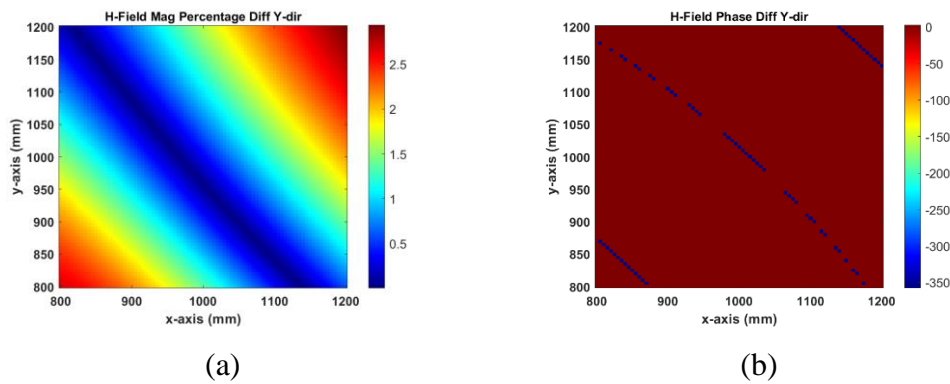
For a PEC sphere that has 1.25λ radius mean magnitude error for E-field is 0.85 percent and for H-field is equal to 1.13 percent. Mean phase error for E-field is equal to 0.33 degrees. For H-field it is equal to -1.02 degrees.

CHAPTER 4

REACTION THEOREM

In this chapter, fundamentals of the reaction theorem will be explained and it will be utilized with the combination of fields found in previous chapters to explain how the interaction between transmitter antenna and the receiver antenna is computed by using them.

Previous chapters of this thesis were actually preliminary work to employ this theorem, which is quite useful to determine and characterize the interaction between the transmitter and receiver antennas. Reaction theorem is fundamental key to determine the coupling between any antennas, has many different forms, that either utilizes electromagnetic fields or electrical circuit quantities like voltage and current. There are also hybrid forms that uses both fields and circuit quantities in a single equation. Reaction theorem is founded over reciprocity principle, which explains the fact that an antenna has same characteristics in transmitting and receiving operations.

Lorentz reciprocity principle which only contains field expressions can be shown as follows:

$$\oint_{S_1} (\bar{E}_1 \times \bar{H}_2 - \bar{E}_2 \times \bar{H}_1) \cdot \overline{dS} = \oint_{S_2} (\bar{E}_2 \times \bar{H}_1 - \bar{E}_1 \times \bar{H}_2) \cdot \overline{dS} \qquad (4.1)$$

Where $\bar{E}_1$ and $\bar{H}_1$ denotes the electric and magnetic fields created by the antenna 1 respectively. Similarly, $\bar{E}_2$ and $\bar{H}_2$ are the electric and magnetic fields created by the antenna 2. S_1 and S_2 are surfaces that enclose antenna 1 and antenna 2, respectively. It should be noted that, surfaces that encloses the antennas must not intersect with each other and must not include any kind of source or scatterer other than antenna itself.

Circuit version of the reciprocity principle can be shown as [25]:

$$V_{12}I_{11} = V_{21}I_{22} \qquad (4.2)$$

Where I_{11} denotes the current at port 1 of the microwave circuit and when it is excited from port 1 as shown in Figure 4.1. Similarly, I_{22} denotes the current at port 2 of the microwave network, when it is excited from port 2. V_{12} is the voltage created at the terminals of port 1 as shown in Figure 4.2. V_{21} is equal to potential difference created at the terminals of port 2. Circuit form of reciprocity principle is stating that for a passive reciprocal microwave device such as coupler, filter or power divider etc. interchanging the input and output ports of such network will not have an impact on response of the network. Meaning that, its transmission characteristics will stay exactly same even if it is fed from different ports. This principle is also valid even if the network itself does not contain any kind of symmetry in its structure.
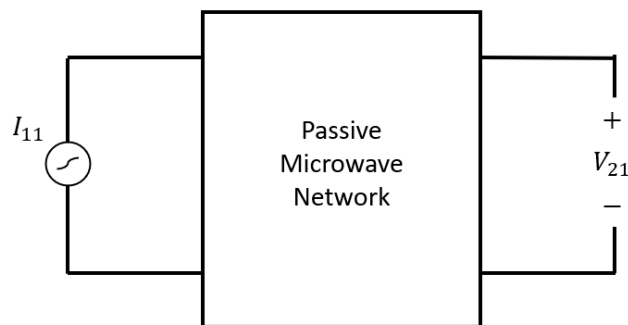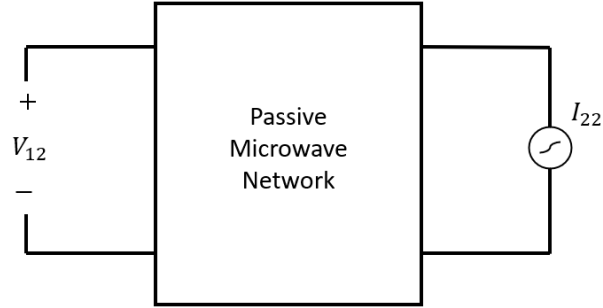

Figure 4.1 Excitation Scenario for Port 1

Figure 4.2 Excitation Scenario for Port 2

In equation (4.1), quantities at right hand side and left-hand side are called as reactions. Left hand side of the equation is denoted by the symbol $\langle 1,2 \rangle$ and defined as reaction of antenna 1 over antenna 2. Similarly for the right-hand side, it is represented as $\langle 2,1 \rangle$ and defined as reaction of antenna 2 over antenna 1 [26].

It is also stated that, left hand side of the equation (4.2) equals to negative of left-hand side of the equation (4.1) which results in following expression [27]:

$$V_{12}I_{11} = - \oint_{S_1} (\bar{E}_1 \times \bar{H}_2 - \bar{E}_2 \times \bar{H}_1) \cdot \overline{dS} \qquad (4.3)$$

Most of the time, reciprocity principle derivations are made for the scenario where both antennas are placed in the same environment. However, even if one of the antennas are positioned in a different medium, a reciprocity theorem can be defined between these two antennas which can be expressed as following [28]:

$$V_{21}I'_{22} = - \oint_{S_2} (\bar{E}'_2 \times \bar{H}_1 - \bar{E}_1 \times \bar{H}'_2) \cdot \overline{dS} \qquad (4.4)$$

In equation (4.4) E'_2 and H'_2 denotes the electric and magnetic field created by antenna 2, respectively, when it is placed in a different medium. I'_{22} is also denoting the current at the input port of antenna 2 when it is excited and transmitting signal. As shown in Figure 4.3 and Figure 4.4, when antenna 1 is excited, it radiates in the presence of the scatterer and the receiver antenna with its port left open, whereas

when antenna 2 is excited, it radiates into free space. Hence $\bar{E}_2'$ and $\bar{H}_2'$ are the fields exported from CST Microwave Studio when a single antenna is radiating into free space.
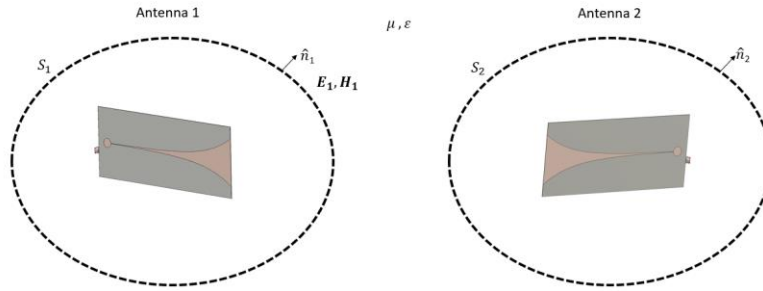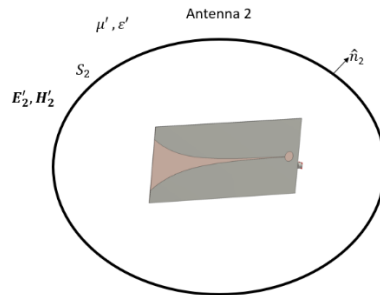

Figure 4.3 Antenna 1 Radiation Scenario

Figure 4.4 Antenna 2 Radiation Scenario (Different Medium)

From now on, since both circuit and electric form of reciprocity is defined and combination of them can be used in single equation, relationship between mutual impedance and reaction quantities can be defined.

Mutual impedance between two antennas can be defined as following:

$$Z_{21} = \left.\frac{V_{21}}{I_{11}}\right|_{I_{21}=0} \tag{4.5}$$

$$= -\frac{\langle 2,1 \rangle}{I_{11}I_{22}'} \tag{4.6}$$

42

Replacing the reaction quantity in equation (4.6) mutual impedance can be found by utilizing the general form of reciprocity theorem as following:

$$Z_{21} = -\frac{1}{I_{11}I'_{22}} \oint_{S_2} (\bar{E}'_2 \times \bar{H}_1 - \bar{E}_1 \times \bar{H}'_2) \cdot \overline{dS} \qquad (4.7)$$

It should be noted that in equation (4.7) fields $\bar{E}_1$ and $\bar{H}_1$ are the fields created by transmitting antenna when both receiver antenna and the scatterer itself are present. In proposed method, those fields are found of the superposition of the fields scattered from the target and the fields radiated by the transmitter antenna at the position of receiver antenna. When calculating the former fields, the incident field is assumed to be the field created by transmitter antenna radiating in free space. Similarly for the later fields, transmitter antenna is assumed to radiate in free space. Therefore, some errors will be introduced because exact fields are not used. In [29] a modified reaction theorem is proposed to account for multi-scattering in order to increase the accuracy of calculations. However, in this work only single scattering is considered since it provides good balance between accuracy, simulation time and memory requirements.

Field quantities are not enough to find the mutual coupling between transmitter and receiver antennas, excitation currents of antennas must be also found. Excitation current quantities I_{11} and I'_{22} are denoting the currents that is created at the ports of transmitter and receiver antennas, when the corresponding antenna is excited with a voltage source. Note that, I_{11} is the current when transmitter antenna is excited in the presence of receiver antenna and the target. However, it is assumed that this quantity is not affected too much with the presence of other objects. In addition to that, since transmitter and receiver antennas are same type, excitation currents for them are assumed to be equal. Therefore, in the calculations, I_{11} and I'_{22} are assumed to be equal.

To find the excitation current, a current monitor tool defined in CST Microwave Studio is used. As in Figure 4.5, the magnetic field along a closed loop is evaluated to compute the current enclosed by the loop.
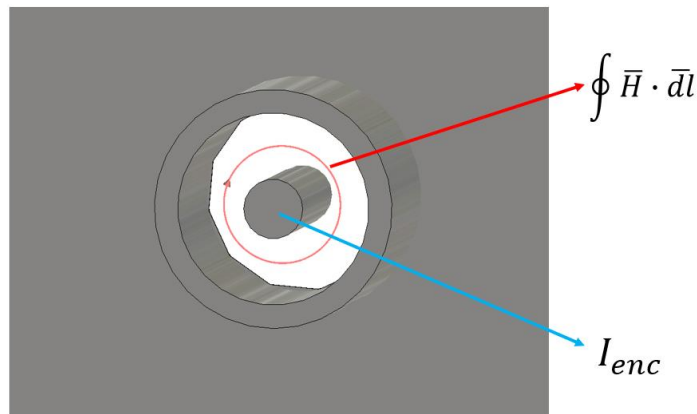

Figure 4.5 Current Monitor Definition in CST

Current that is created at the excitation port of the patch antenna with respect to frequency is given in Figure 4.6:
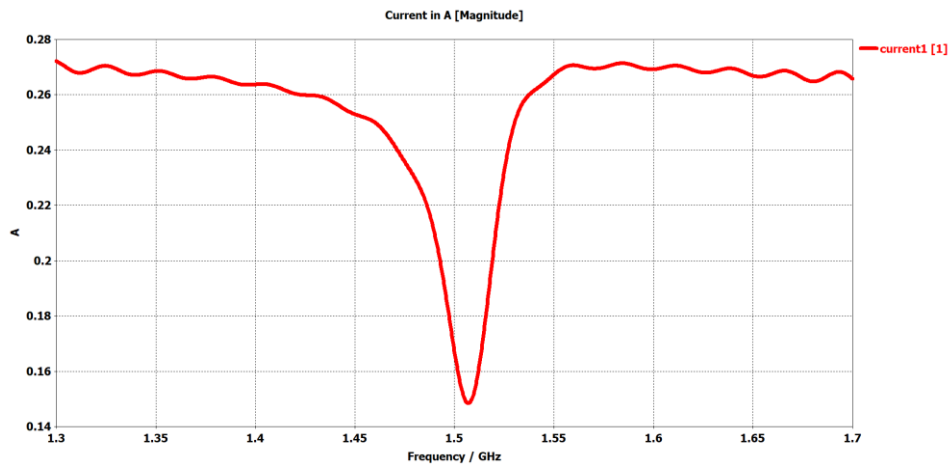

Figure 4.6 Excitation Current with respect to Frequency

Now all the quantities to find mutual impedance between transmitter and receiver antennas are available. Hence, result of the approach proposed in this thesis can be compared with the results of the full-wave simulation of the transmitter and receiver antennas and the target. The interaction between two antennas is computed by the

proposed method when there is no scatterer. First, the incident field is computed by using only $1.5\lambda \times 1.5\lambda$ (300mm × 300mm) size surface positioned 10mm away from the transmitter and receiver antennas.
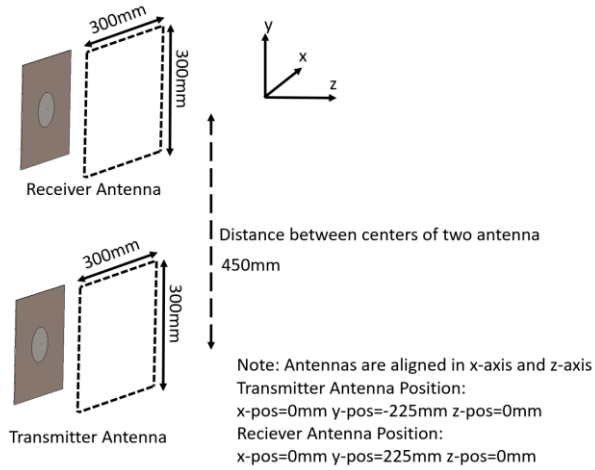
Figure 4.7: Validation Scenario for the proposed method (Only Front Surface)

Z_{21} values are obtained by the proposed method are compared to the results of CST simulations in Figure 4.8 - Figure 4.10.
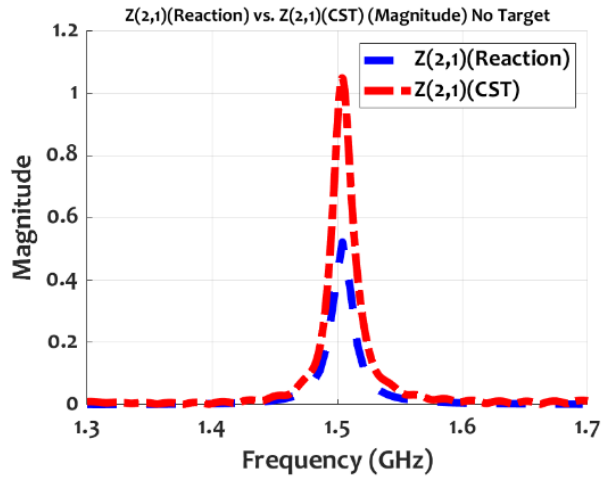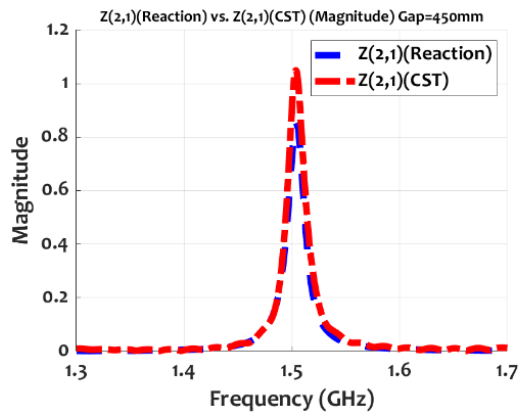

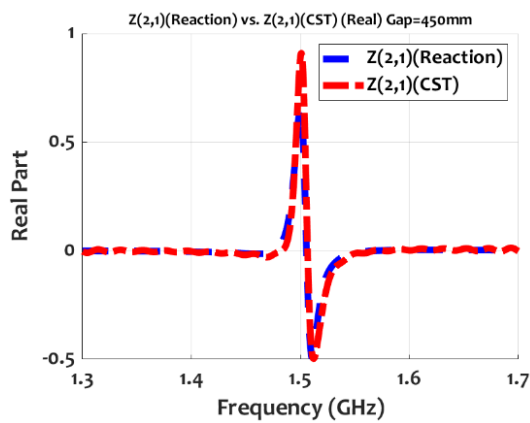Figure 4.8: Z(2,1) Magnitude Comparison (CST vs Reaction Theorem) (Front Surface only)
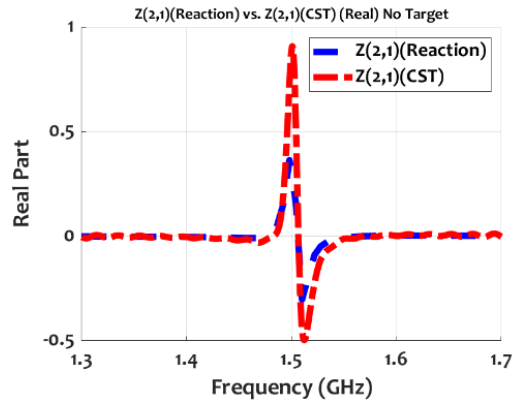
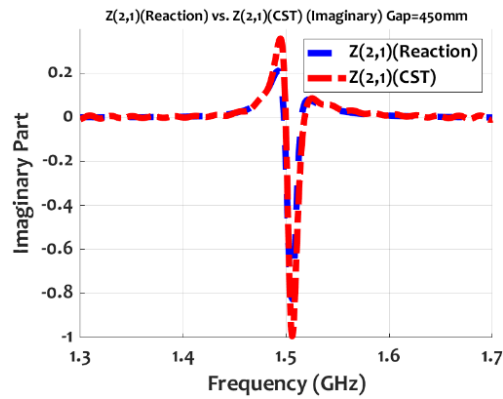Figure 4.9: Z(2,1) Real Part Comparison (CST vs Reaction Theorem) (Front Surface only)
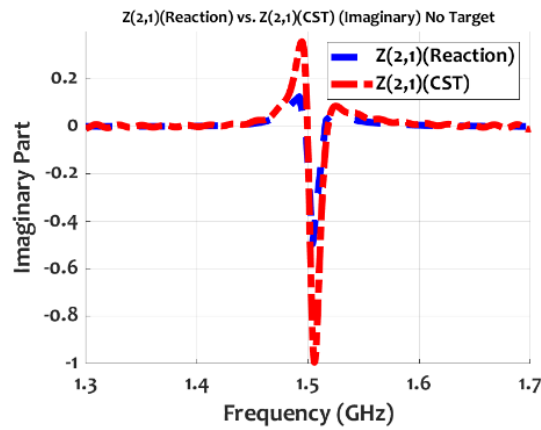
Figure 4.10: Z(2,1) Imaginary Part Comparison (CST vs Reaction Theorem) (Front Surface only)

As it can be seen from Figure 4.8 to Figure 4.10 even though using only front surface was giving good results to compute incident field, Z_{21} values obtained by using only front surface are not accurate enough. Because application of reaction theorem requires a closed surface for integration.

Same scenario is repeated but now, all surfaces on a rectangular prism except the back surface are used both to find incident field and apply reaction theorem. That scenario is shown in Figure 4.11.
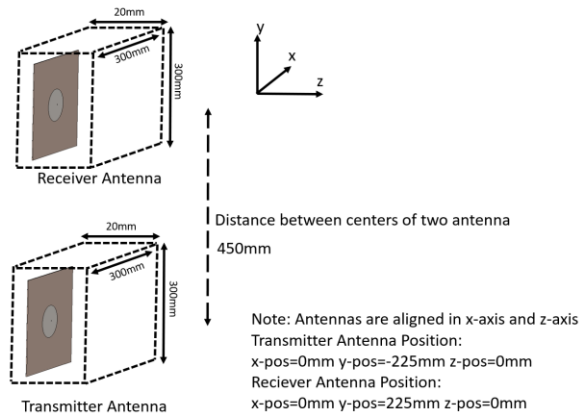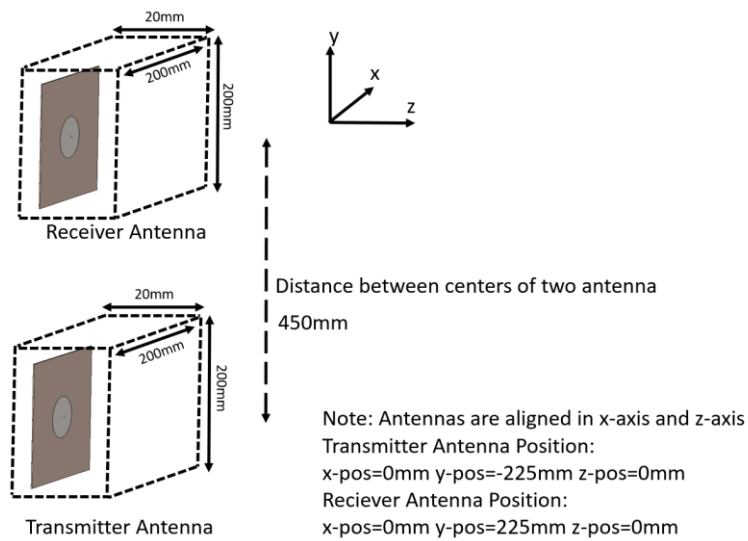
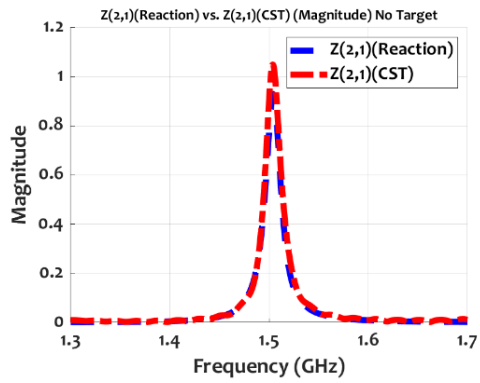Figure 4.11: Validation Scenario for the proposed method (No Back Surface)

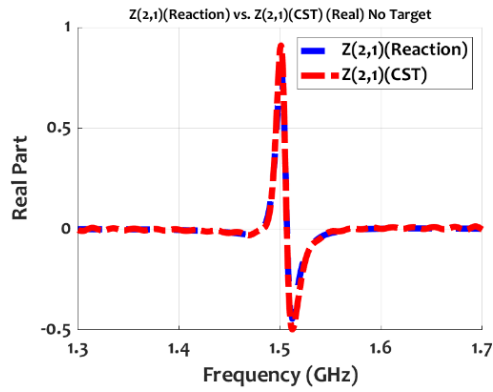Figure 4.12: Z(2,1) Magnitude Comparison (CST vs Reaction Theorem) (No Back Surface)

Figure 4.13: Z(2,1) Real Part Comparison (CST vs Reaction Theorem) (No Back Surface)

Figure 4.14: Z(2,1) Imaginary Part Comparison (CST vs Reaction Theorem) (No Back Surface)

As it can be seen, accuracy in magnitude is increased significantly. Since this kind of surface will take some time for computation, the size of the front surface is reduced to 200mm from 300mm length and width to see if it has significant impact on accuracy.

Figure 4.15: Validation Scenario for the proposed method (No Back Surface) (Smaller Front Surface)

Figure 4.16: Z(2,1) Magnitude Comparison (CST vs Reaction Theorem) (No Back Surface)(Small Front Surface)

Figure 4.17: Z(2,1) Real Part Comparison (CST vs Reaction Theorem) (No Back Surface)(Small Front Surface)
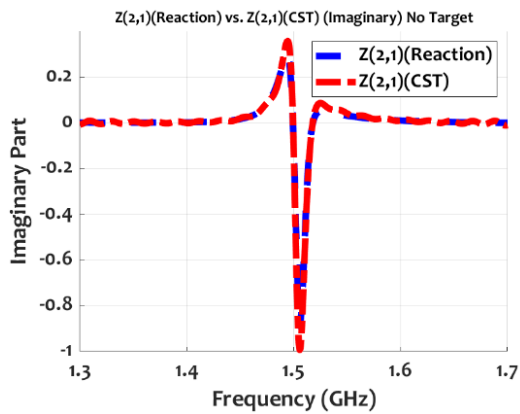
Figure 4.18: Z(2,1) Imaginary Part Comparison (CST vs Reaction Theorem) (No Back Surface)(Small Front Surface)

Accuracy of the calculation compared to CST does not change much even though smaller surface is used to calculate mutual impedance. This shows that emphasis on closed surface is more important than usage of larger surfaces for accuracy. One last change over surface is implemented to see the impact over accuracy. Side surfaces are extended to back of antenna from 20mm to 100 mm.
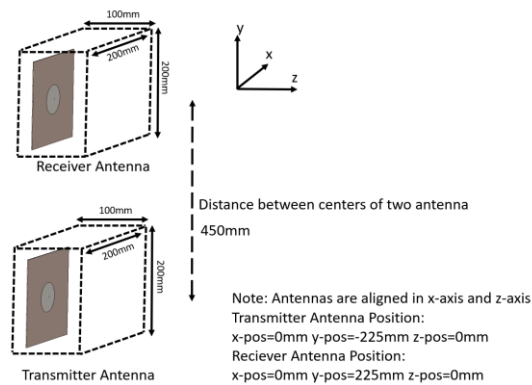
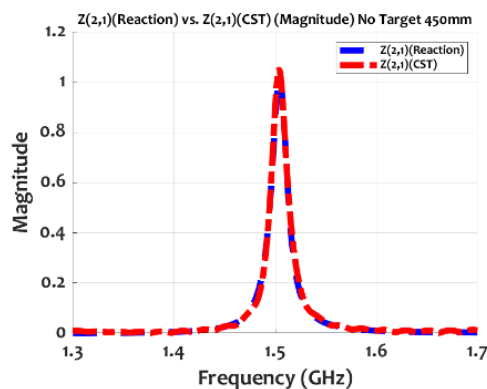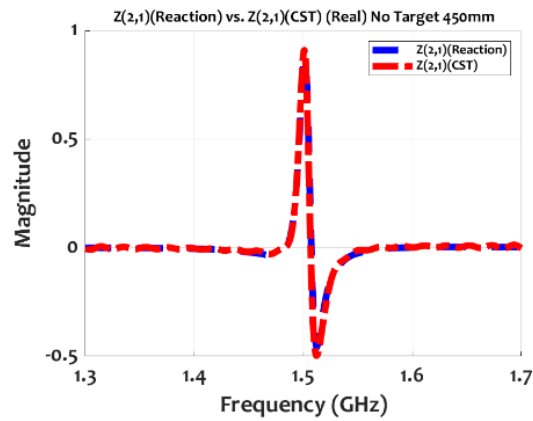Figure 4.19: Z(2,1) Comparison Scenario (No Back Surface) (Larger Side Surfaces)

Figure 4.20: Z(2,1) Magnitude Comparison (CST vs Reaction Theorem) (No Back Surface)(Larger Side Surfaces)

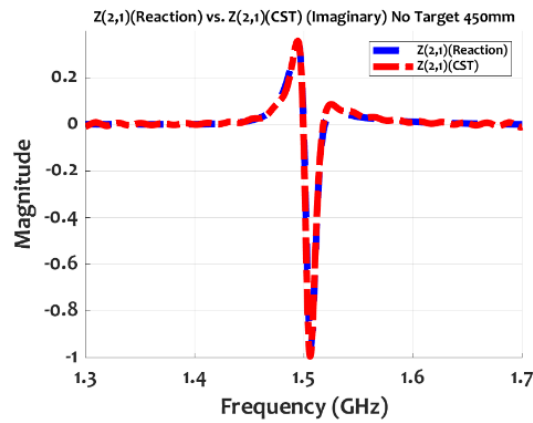Figure 4.21: Z(2,1) Real Part Comparison (CST vs Reaction Theorem) (No Back Surface) (Larger Side Surfaces)

Figure 4.22: Z(2,1) Imaginary Part Comparison (CST vs Reaction Theorem) (No Back Surface) (Bigger Side Surfaces)

It can be seen that, this configuration provides almost identical results with CST, hence this surface will be used for further examination of different cases.

To investigate limits of the proposed approach, distance between antennas is decreased from 450mm to 350mm and 250mm as shown in Figure 4.23.
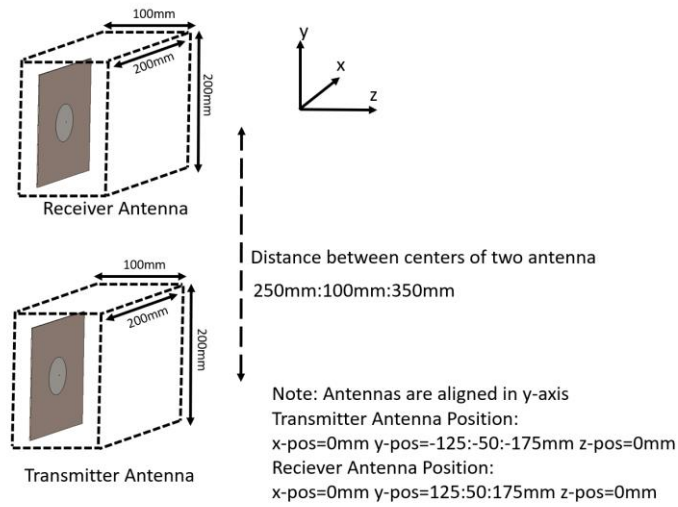
Figure 4.23: Z(2,1) Comparison Scenario (CST vs Reaction Theorem) (Varying Distances)

The results for 350mm distance are presented and compared in Figure 4.24 - Figure 4.26, whereas results for 250mm distance are compared in Figure 4.27 - Figure 4.29.
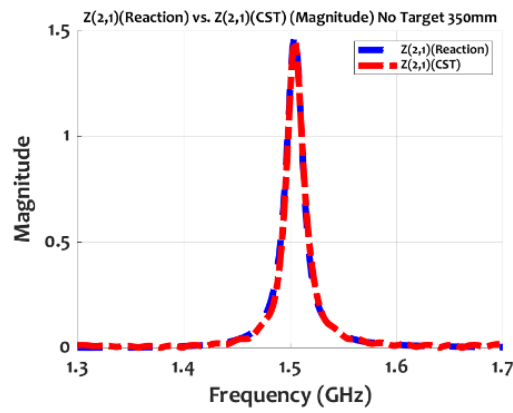

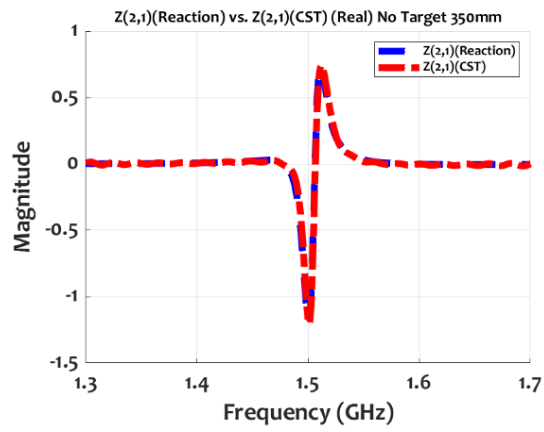Figure 4.24: Z(2,1) Magnitude Comparison (CST vs Reaction Theorem) (350 mm Gap)

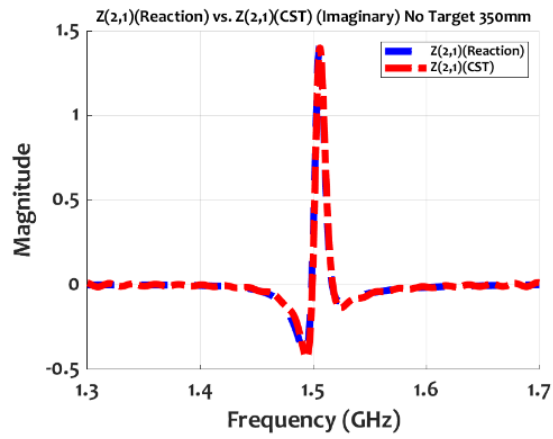Figure 4.25: Z(2,1) Real Part Comparison (CST vs Reaction Theorem) (350 mm Gap)

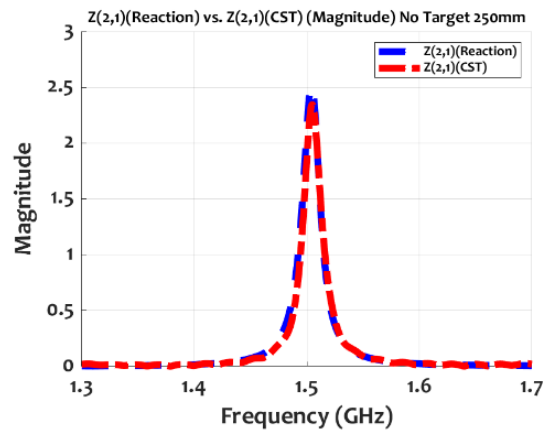Figure 4.26: Z(2,1) Imaginary Part Comparison (CST vs Reaction Theorem) (350 mm Gap)

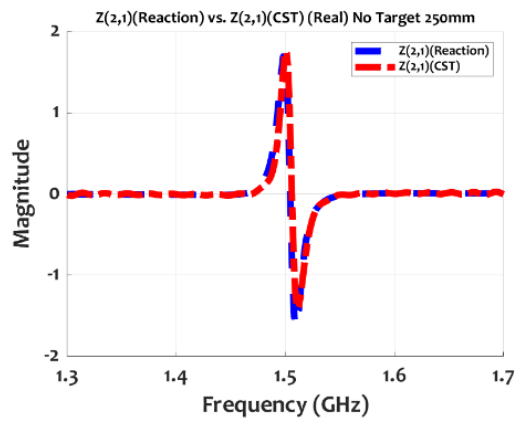Figure 4.27: Z(2,1) Magnitude Comparison (CST vs Reaction Theorem) (250 mm Gap)

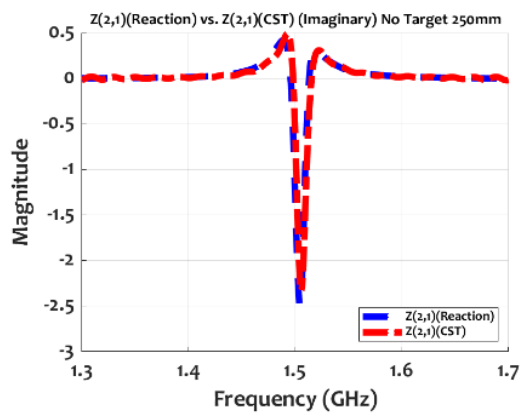Figure 4.28: Z(2,1) Real Part Comparison (CST vs Reaction Theorem) (250 mm Gap)

Figure 4.29: Z(2,1) Imaginary Part Comparison (CST vs Reaction Theorem) (250 mm Gap)

For a better comparison, magnitude of Z_{21} at 1.5 GHz computed for three different distance values between antennas (denoted as Gap) are presented in Figure 4.30.

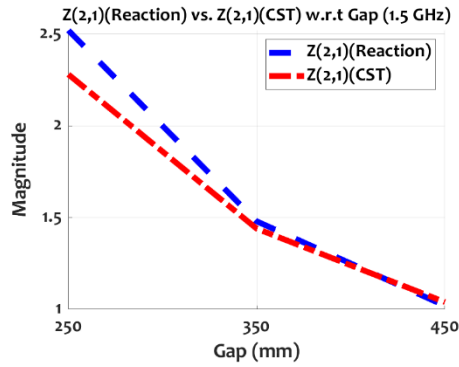Figure 4.30: Z(2,1) Magnitude Comparison with respect to Gap (CST vs Reaction Theorem)

Results shows that when distance between antennas decreases, accuracy also decreases. Because as antennas get closer, they are affecting their radiation characteristics more. Also, small dipole approximation gets less accurate as the observation distance is decreasing. Even then, proposed method still provides acceptable results when distance between closest points of antennas is roughly equal to quarter wavelength.

Another scenario is constructed for comparison. This time antennas are put side by side instead of on top of each other. The box size and distance between antennas can be seen in Figure 4.31 and the results of this case are presented in Figure 4.32 - Figure 4.34.
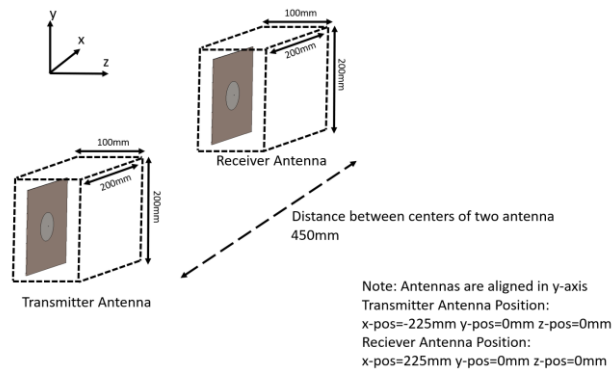
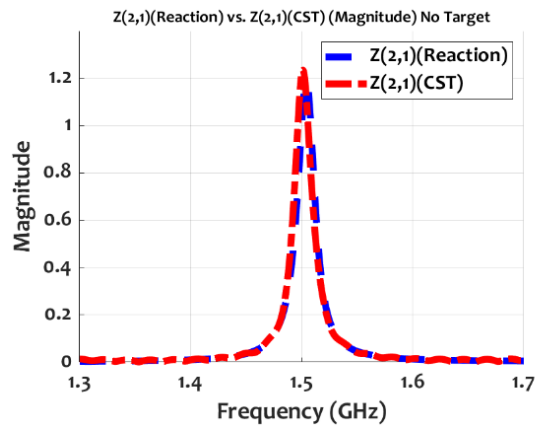Figure 4.31: Z(2,1) Comparison Scenario (CST vs Reaction Theorem) (Side by side Antennas)

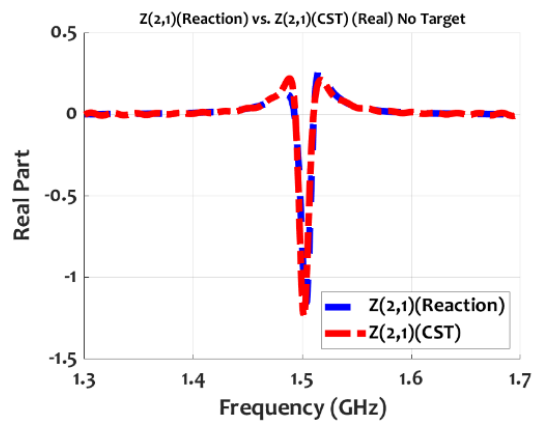Figure 4.32: Z(2,1) Magnitude Comparison (CST vs Reaction Theorem) (Side by Side Antennas)

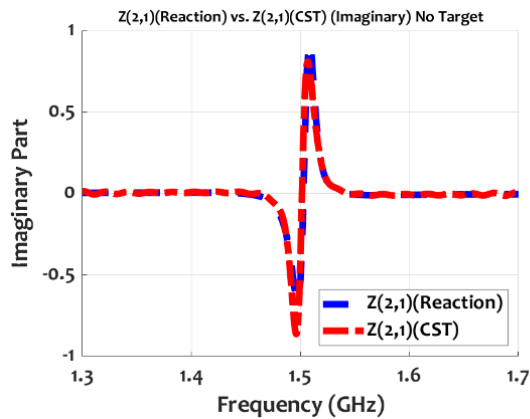Figure 4.33: Z(2,1) Real Part Comparison (CST vs Reaction Theorem) (Side by Side Antennas)

Figure 4.34: Z(2,1) Imaginary Part Comparison (CST vs Reaction Theorem) (Side by Side Antennas)

The proposed method provides satisfactory results as well for side-by-side placement.

Now that comparisons are made for many different scenarios, PEC scatterers are included in comparisons. Firstly, a PEC sphere is included as shown in Figure 4.35 and comparisons are made with CST results for 3 different gap values.
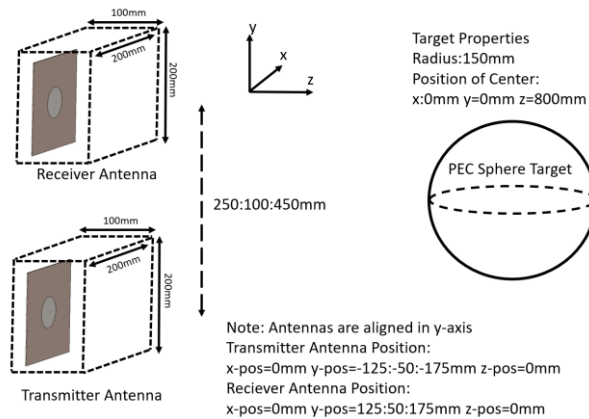

Figure 4.35: Z(2,1) Comparison Scenario (CST vs Reaction Theorem) (PEC Sphere Included)(Varying Distance with Antennas)

The results for 450mm gap are presented in Figure 4.36 - Figure 4.38. The results for 350mm gap are presented in Figure 4.39 - Figure 4.41. And the results for 250mm gap are presented in Figure 4.42 - Figure 4.44.
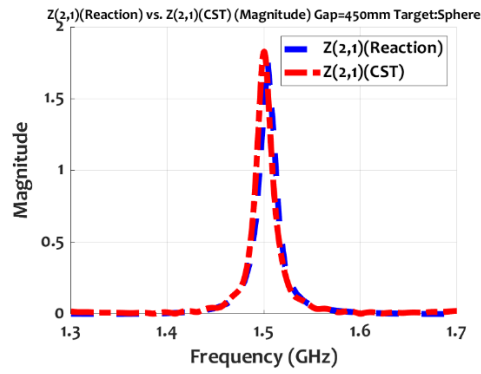
Figure 4.36: Z(2,1) Magnitude Comparison (CST vs Reaction Theorem) (Sphere Target) (450 mm Distance Between Antennas)
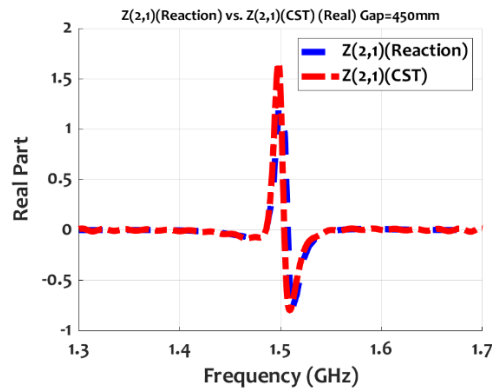

Figure 4.37: Z(2,1) Real Part Comparison (CST vs Reaction Theorem) (Sphere Target) (450 mm Distance Between Antennas)

Figure 4.38: Z(2,1) Imaginary Part Comparison (CST vs Reaction Theorem) (Sphere Target) (450 mm Distance Between Antennas)
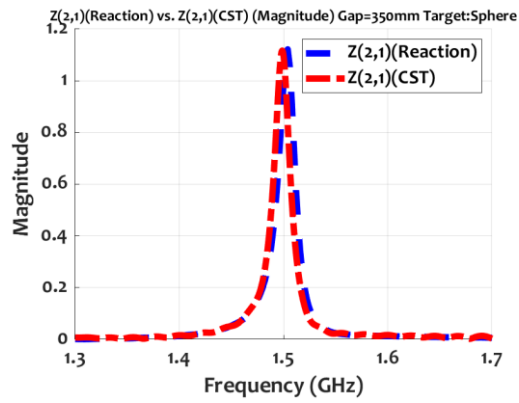
Figure 4.39: Z(2,1) Magnitude Comparison (CST vs Reaction Theorem) (Sphere Target) (350 mm Distance Between Antennas)
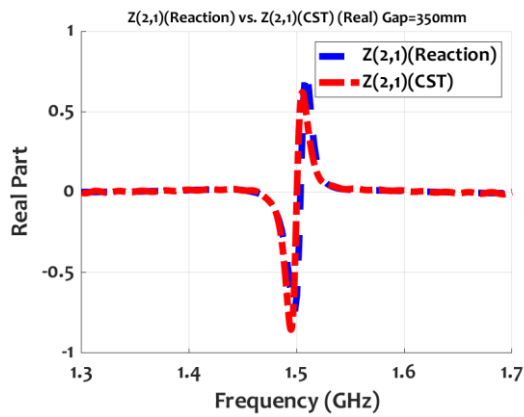
Figure 4.40: Z(2,1) Real Part Comparison (CST vs Reaction Theorem) (Sphere Target) (350 mm Distance Between Antennas)
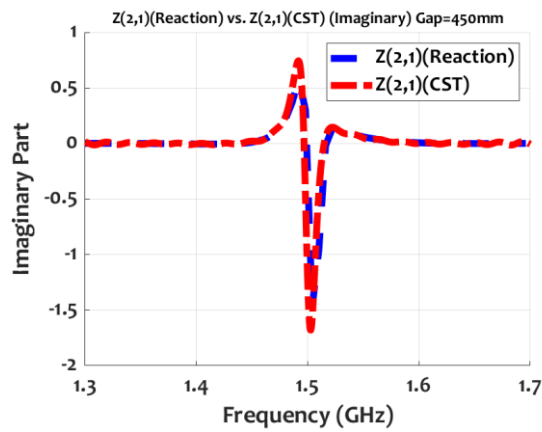

Figure 4.41: Z(2,1) Imaginary Part Comparison (CST vs Reaction Theorem) (Sphere Target) (350 mm Distance Between Antennas)

Figure 4.42: Z(2,1) Magnitude Comparison (CST vs Reaction Theorem) (Sphere Target) (250 mm Distance Between Antennas)

Figure 4.43: Z(2,1) Real Part Comparison (CST vs Reaction Theorem) (Sphere Target) (250 mm Distance Between Antennas)

Figure 4.44: Z(2,1) Imaginary Part Comparison (CST vs Reaction Theorem) (Sphere Target) (250 mm Distance Between Antennas)
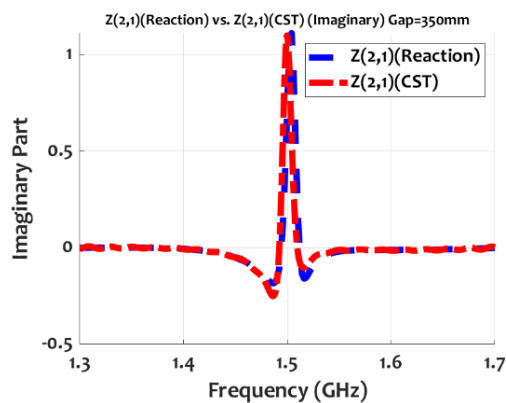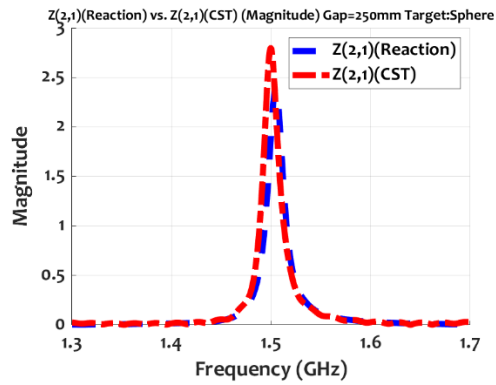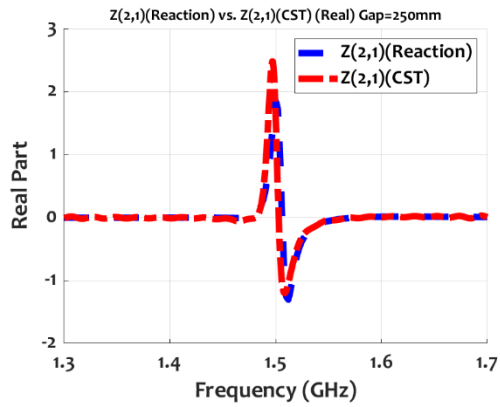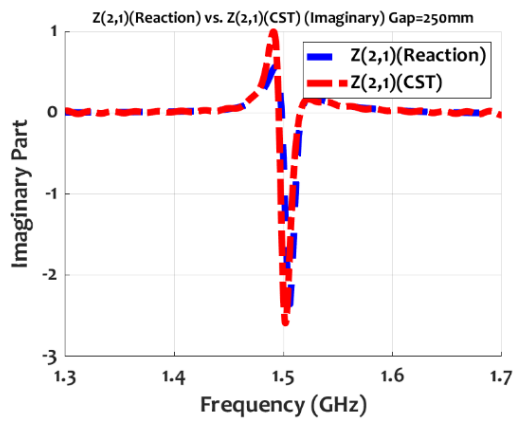
As the distance between antennas are getting close to each other, it can be seen that results of the proposed method start to deviate from CST results, because assumption of scatterer and transmitter radiating into free-space is getting less valid and multi-scatterings are getting stronger.

To investigate the effects of changing the distance between target and antennas it is first increased to 1000mm from 800mm, then it is decreased to 600mm. The results for 1000mm distance are shown in Figure 4.46 - Figure 4.48 and the results for 600mm distance are shown in Figure 4.49 - Figure 4.51.
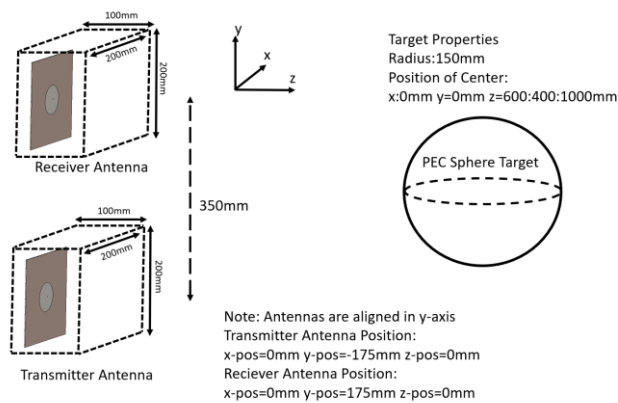
Figure 4.45: Z(2,1) Comparison Scenario (CST vs Reaction Theorem) (PEC Sphere Included)(Varying Distance of Target)

Figure 4.46: Z(2,1) Magnitude Comparison (CST vs Reaction Theorem) (Sphere Target) (1000 mm Distance Between Antennas and Target)

Figure 4.47: Z(2,1) Real Part Comparison (CST vs Reaction Theorem) (Sphere Target) (1000 mm Distance Between Antennas and Target)

Figure 4.48: Z(2,1) Imaginary Part Comparison (CST vs Reaction Theorem) (Sphere Target) (1000 mm Distance Between Antennas and Target)
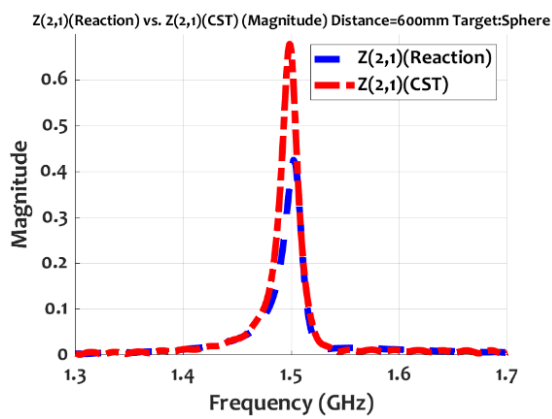
Figure 4.49: Z(2,1) Magnitude Comparison (CST vs Reaction Theorem) (Sphere Target) (600 mm Distance Between Antennas and Target)
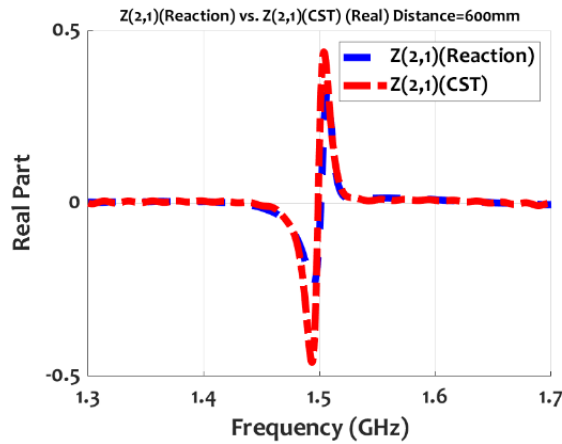
Figure 4.50: Z(2,1) Real Part Comparison (CST vs Reaction Theorem) (Sphere Target) (600 mm Distance Between Antennas and Target)
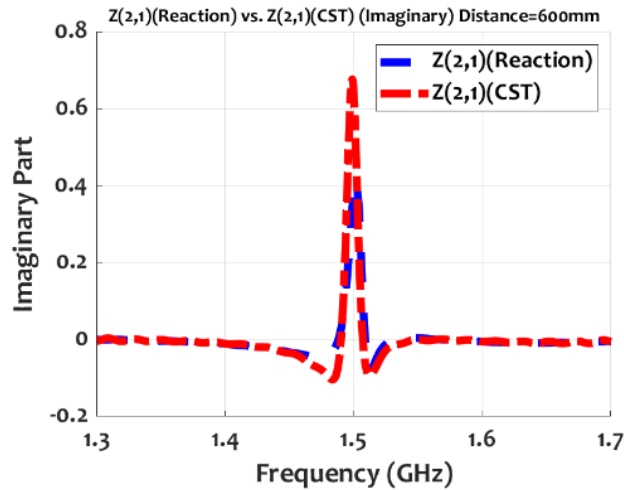
Figure 4.51: Z(2,1) Imaginary Part Comparison (CST vs Reaction Theorem) (Sphere Target) (600 mm Distance Between Antennas and Target)

As expected, as target gets closer, accuracy of proposed method is decreasing since multi-scattering is getting more significant.

Different targets are also examined to see accuracy and effectiveness of the proposed method for various scenarios. First a cone target is considered as shown in Figure 4.52 and results are presented in Figure 4.53 - Figure 4.55. Then a square plate target is considered as shown in Figure 4.56 and results for this target are shown in Figure 4.57 - Figure 4.59.
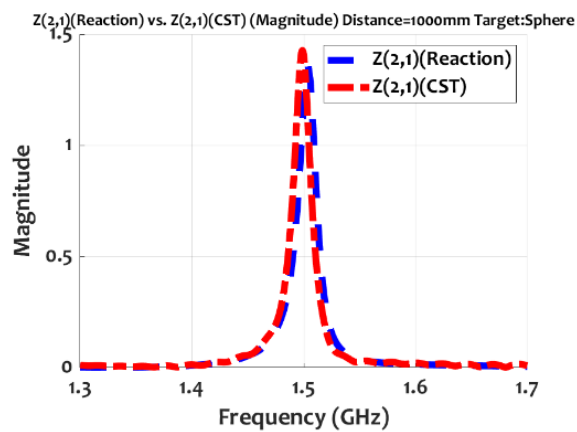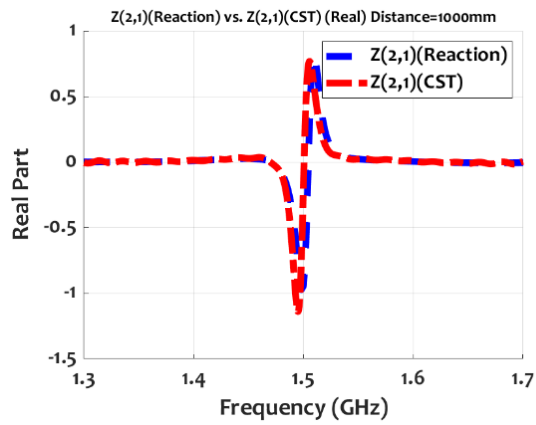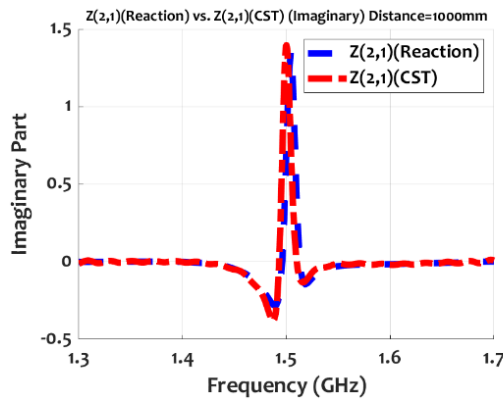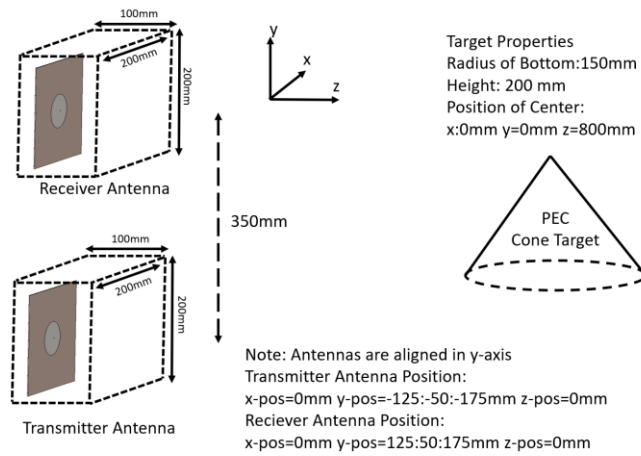
Figure 4.52: Z(2,1) Comparison Scenario (CST vs Reaction Theorem) (PEC Cone)
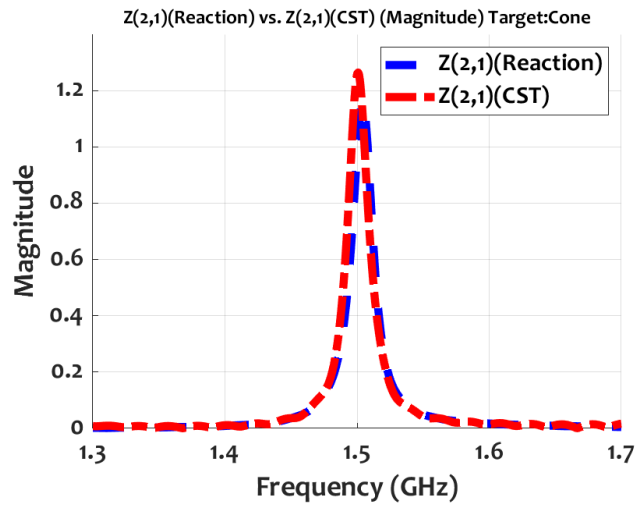
Figure 4.53: Z(2,1) Magnitude Comparison (CST vs Reaction Theorem) (Cone Target)
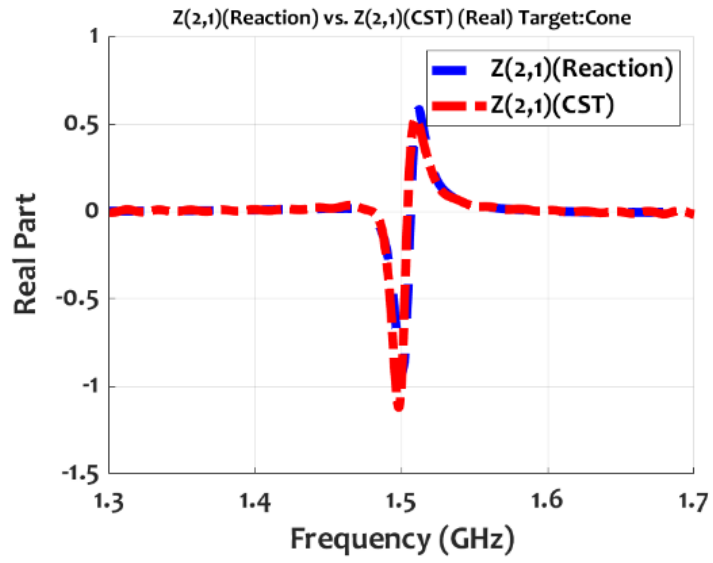
Figure 4.54: Z(2,1) Real Part Comparison (CST vs Reaction Theorem) (Cone Target)
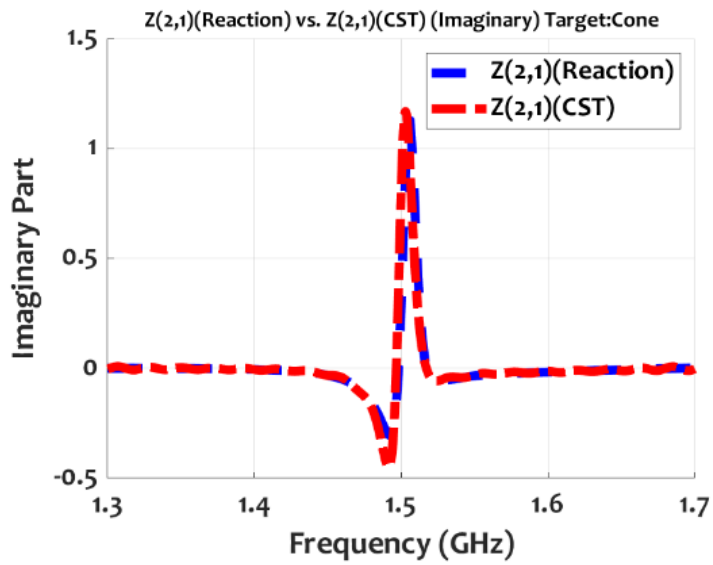
Figure 4.55: Z(2,1) Imaginary Part Comparison (CST vs Reaction Theorem) (Cone Target)
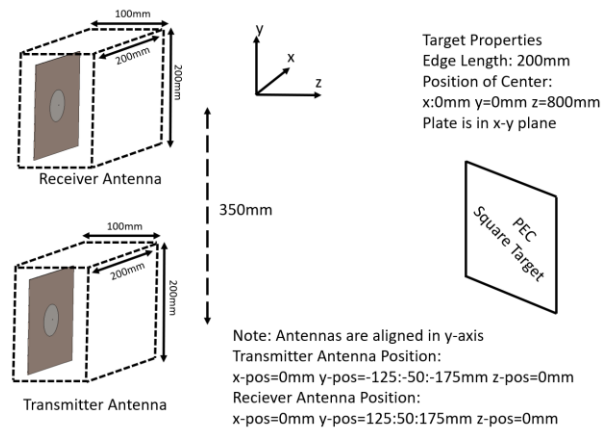
Figure 4.56: Z(2,1) Comparison Scenario (CST vs Reaction Theorem) (PEC Plate)
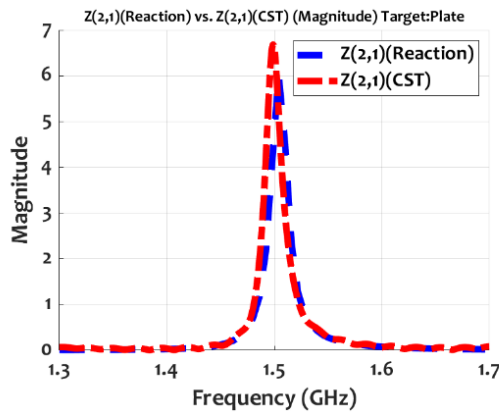
Figure 4.57: Z(2,1) Magnitude Comparison (CST vs Reaction Theorem) (Plate Target)
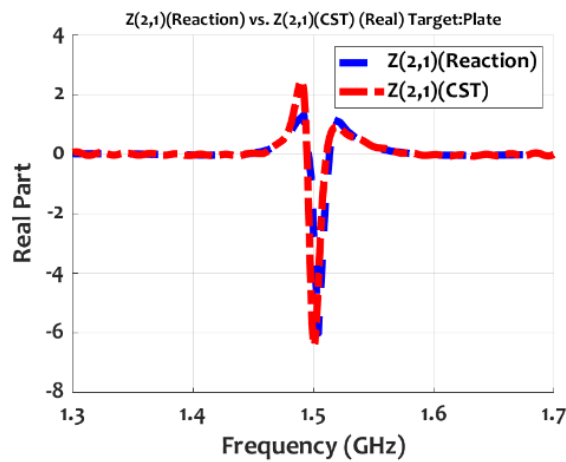
Figure 4.58: Z(2,1) Real Part Comparison (CST vs Reaction Theorem) (Plate Target)
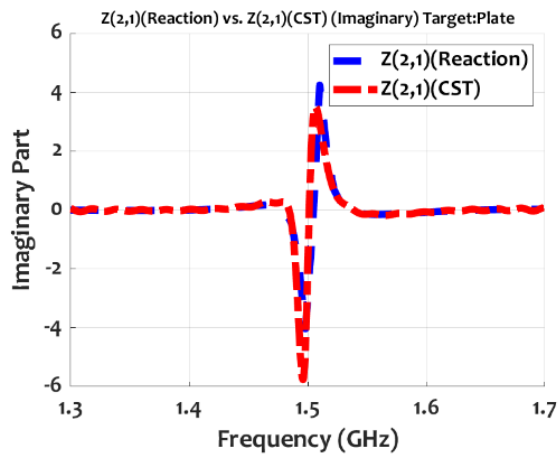
Figure 4.59: Z(2,1) Imaginary Part Comparison (CST vs Reaction Theorem) (Plate Target)

To see the effect of different targets, results of Z(2,1) for different target are shown in at the same time in Figure 4.60 - Figure 4.62. Impact of square plate is much higher to Z(2,1) parameter so in Figure 4.63 - Figure 4.65 only sphere and cone targets are plotted to show their differences more clearly.
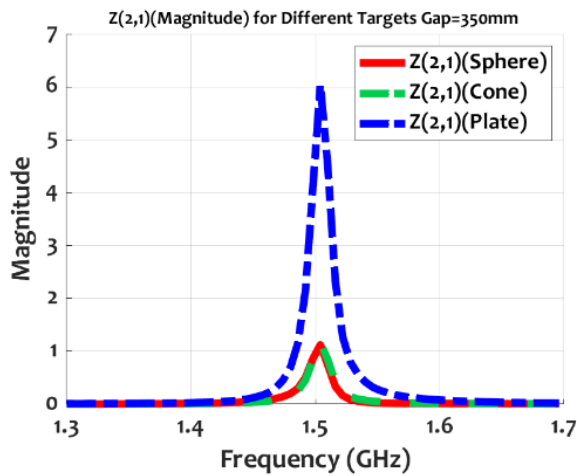
Figure 4.60 Z(2,1) Magnitude Comparison for Different Targets
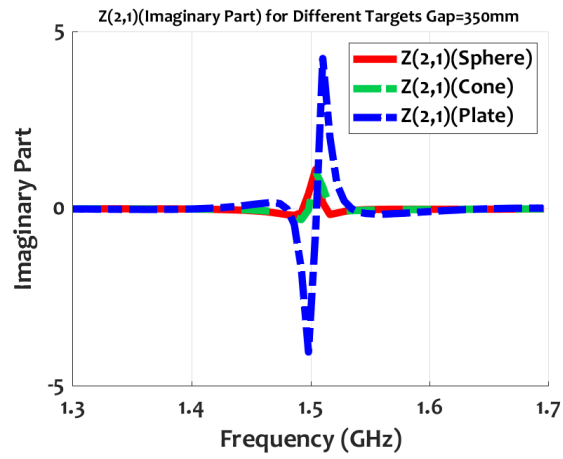
Figure 4.61:Z(2,1) Real Part Comparison for Different Targets
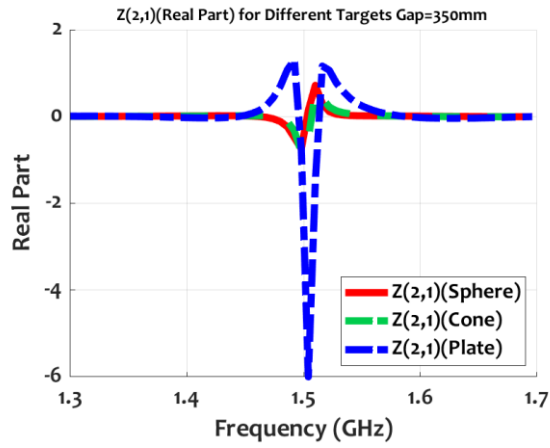
Figure 4.62: Z(2,1) Imaginary Part Comparison for Different Targets
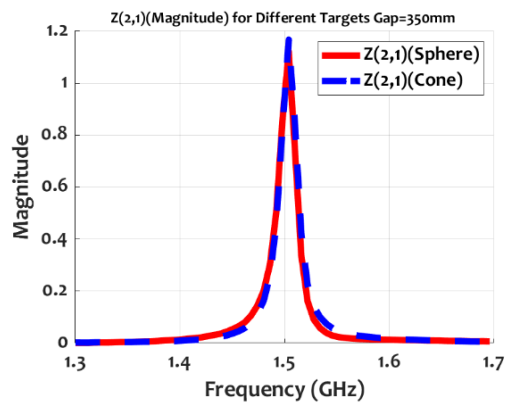
Figure 4.63 Z(2,1) Magnitude Comparison for Sphere and Cone Targets
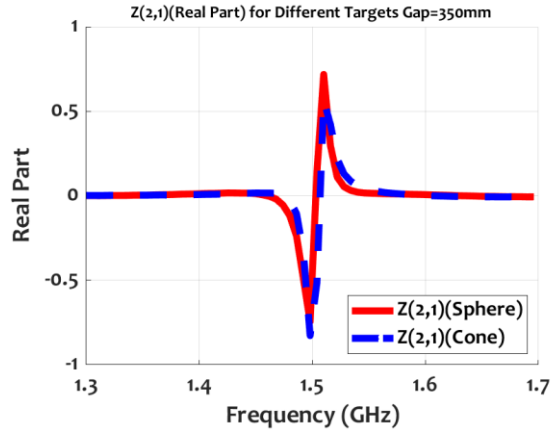
Figure 4.64:Z(2,1) Real Part Comparison for Sphere and Cone Targets
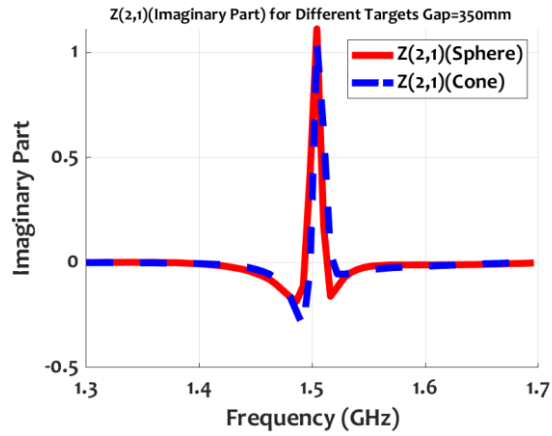
Figure 4.65: Z(2,1) Imaginary Part Comparison for Sphere and Cone Targets

As it can be seen from Figure 4.63 to Figure 4.65, since reflections from targets are very low, direct coupled fields dominate the total received signal and consequently, the difference between scattering characteristics of sphere and cone targets are not noticeable. To make a better comparison between different targets, only the scattered fields need to be compared. Elimination of the direct field from the total field can be achieved by converting Z-parameters to S-parameters. Since S_{12} values obtained in the absence of a target give the direct coupled fields, the difference in S_{12} values obtained in the presence and absence of the scaterrer will give the scattered fields due to scatterer as shown in equation (4.8).

$$S(2,1)_{total} - S(2,1)_{notarget} \approx S(2,1)_{scatterer} \tag{4.8}$$

Therefore first, S-parameters of two antenna system are evaluated when no target is present and distance between antenna centers is equal to 350 mm. Then S-parameters of two antenna system are evaluated when sphere, cone and square plate targets are present, as shown in their respective scenarios in Figure 4.35, Figure 4.52 and Figure 4.56.

To calculate the S-parameters, all the Z-parameter values must be known between two antennas. However, only mutual impedance (Z_{21}) can be calculated with proposed method. Using the reciprocity theorem, it can be said that Z_{21} and Z_{12} are equal to each other in an isotropic, homogenous free space. Self impedance values of antennas (Z_{11}) can also be extracted from the full-wave simulation performed in CST to calculate near field values of the antenna. In proposed method, it is assumed that all antennas in the system are exactly same, so it can be said that Z_{11} and Z_{22} are equal to each other. Thus, for a two antenna system, calculation of Z_{21} with the proposed method is enough to evaluate S-parameters.

$S(2,1)_{scatterer}$ values for different targets are calculated from both CST results and the results of the proposed method. They are compared for sphere target in Figure 4.66 and Figure 4.69, for cone target in Figure 4.67 and Figure 4.70, and for square plate target in Figure 4.68 and Figure 4.71. It can be concluded that when only scattered fields are considered, different scattering characteristics of different targets can be easily observed. Moreover, although the amplitude of the scattered field is low and ripples are present in the graphs, the results of proposed method agree quite well with CST results.
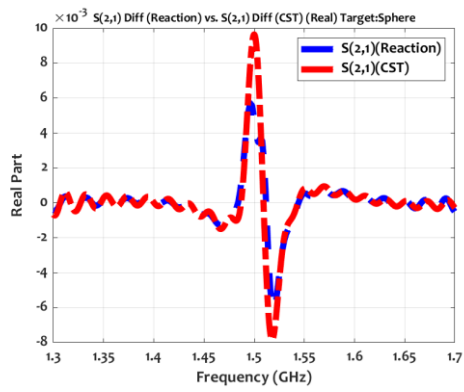
Figure 4.66: Real Part of $S(2,1)_{scatterer}$ for Sphere Target
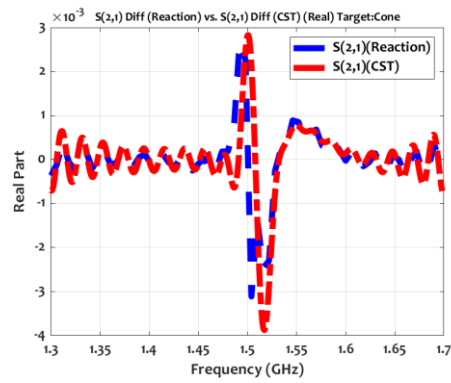
Figure 4.67: Real Part of $S(2,1)_{scatterer}$ for Cone Target
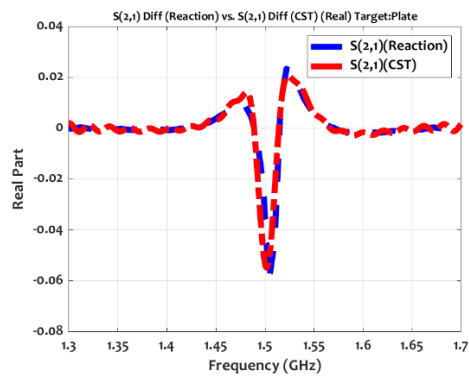
Figure 4.68: Real Part of $S(2,1)_{scatterer}$ for Square Plate Target
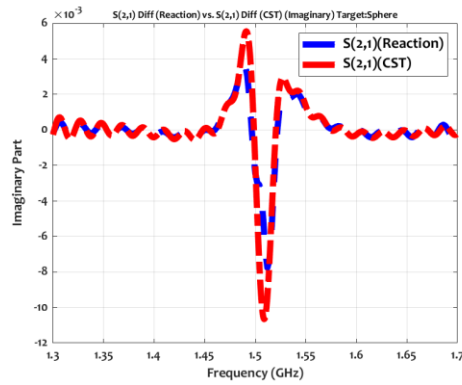
Figure 4.69: Imaginary Part of $S(2,1)_{scatterer}$ for Sphere Target
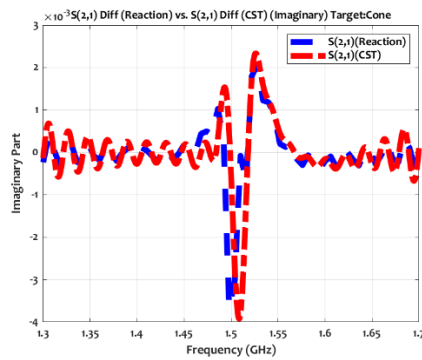
Figure 4.70: Imaginary Part of $S(2,1)_{scatterer}$ for Cone Target
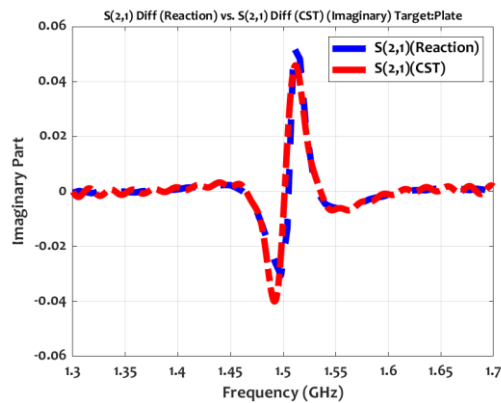
Figure 4.71: Imaginary Part of $S(2,1)_{scatterer}$ for Square Plate Target

Lastly, a 4-antenna system as shown in Figure 4.72 is studied in the presence of a spherical scatterer. Antenna 1 is excited and mutual impedance values between this

antenna and other 3 antennas are calculated. The mutual impedance results between top and bottom antennas (Z_{21}) are presented in Figure 4.73 to Figure 4.75. The mutual impedance results between diagonally placed antennas (Z_{31}) are compared in Figure 4.76 to Figure 4.78. Finally, Figure 4.79 to Figure 4.81 summarize the results for the mutual impedance between side by side antennas (Z_{41}).
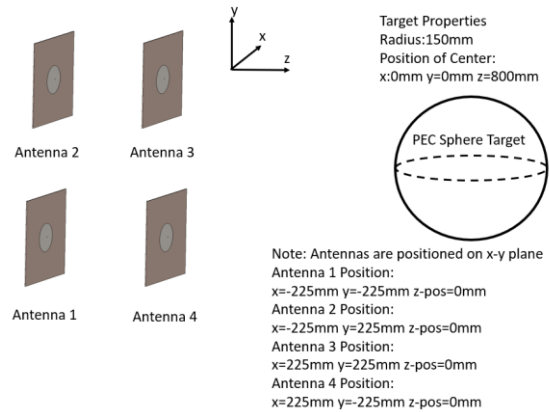
Figure 4.72: Comparison Scenario with Target and 4-antennas (450mm spacing)

Figure 4.73: Z(2,1) Magnitude Comparison for 4 Antennas with 450mm spacing and a Sphere Target

Figure 4.74: Z(2,1) Real Part Comparison for 4 Antennas with 450mm spacing and a Sphere Target

Figure 4.75: Z(2,1) Imaginary Part Comparison for 4 Antennas with 450mm spacing and a Sphere Target
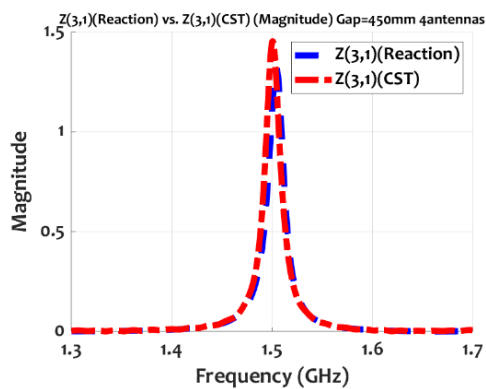
Figure 4.76: Z(3,1) Magnitude Comparison for 4 Antennas with 450mm spacing and a Sphere Target
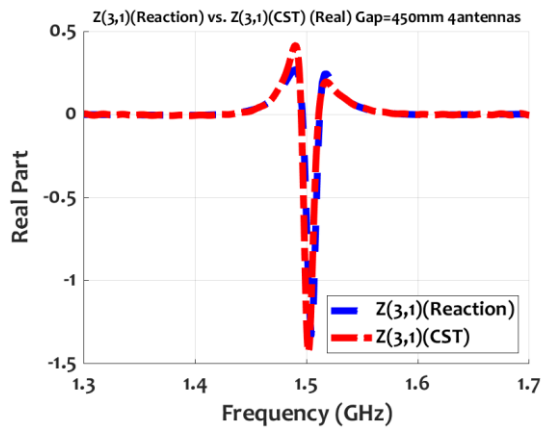
Figure 4.77: Z(3,1) Real Part Comparison for 4 Antennas with 450mm spacing and a Sphere Target
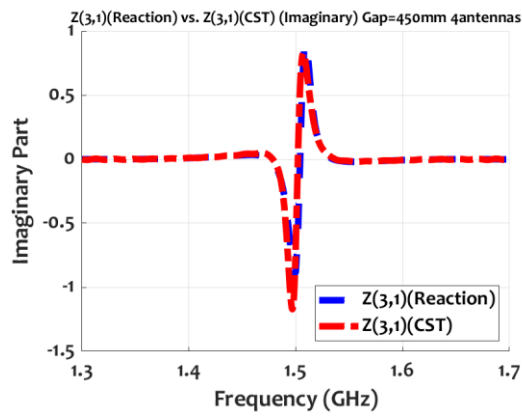
Figure 4.78: Z(3,1) Imaginary Part Comparison for 4 Antennas with 450mm spacing and a Sphere Target
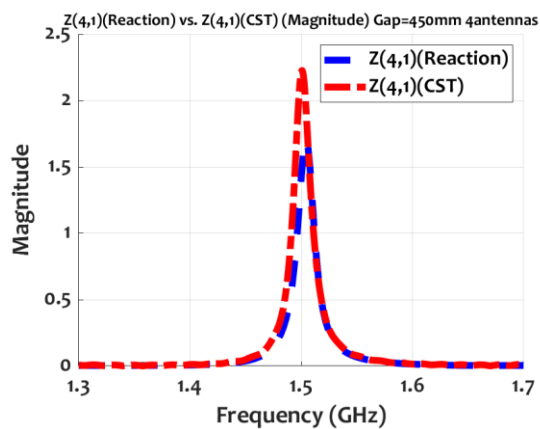
Figure 4.79: Z(4,1) Magnitude Comparison for 4 Antennas with 450mm spacing and a Sphere Target
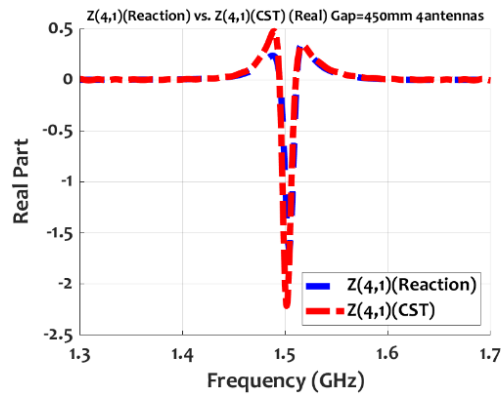
Figure 4.80: Z(4,1) Real Part Comparison for 4 Antennas with 450mm spacing and a Sphere Target
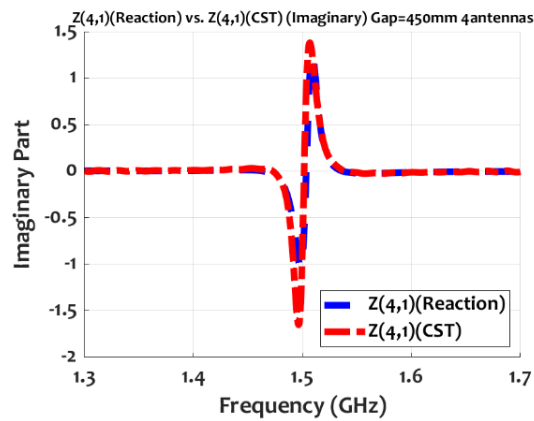
Figure 4.81: Z(4,1) Imaginary Part Comparison for 4 Antennas with 450mm spacing and a Sphere Target

Mutual impedance results for all antennas computed by the proposed method, follow same frequency dependent behavior obtained by CST simulations. However, differences between the peak values are observed.

To understand accuracy limitation of this 4-antenna scenario, antennas in the system are positioned closer to each other such that center to center spacing of the antennas is reduced from 450mm to 350mm and mutual impedance between antenna 1 and antenna 3 is observed.
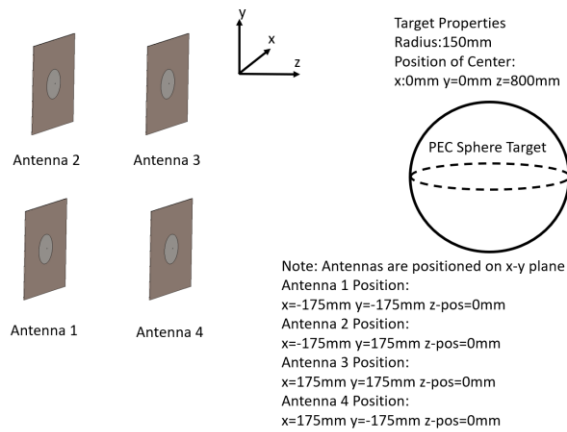
Figure 4.82: Comparison Scenario with Target and 4-antennas (350mm spacing)

Simulation result comparisons for scenario in Figure 4.82 are given in Figure 4.83 - Figure 4.85.
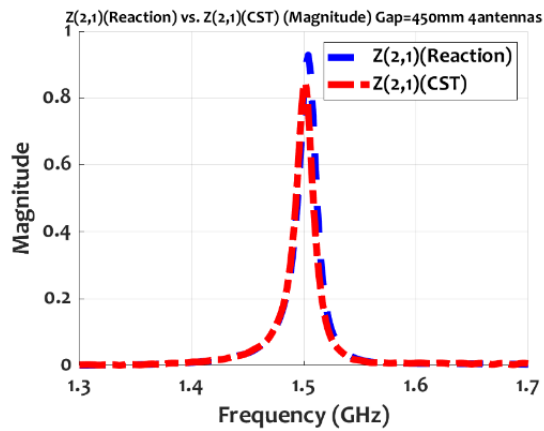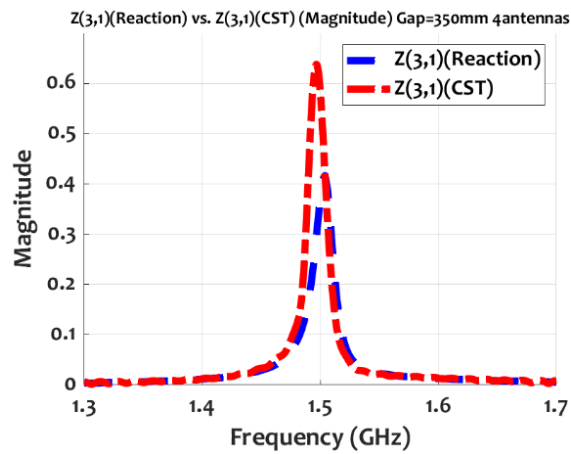

Figure 4.83: Z(3,1) Magnitude Comparison for 4 Antennas with 350mm spacing and a Sphere Target
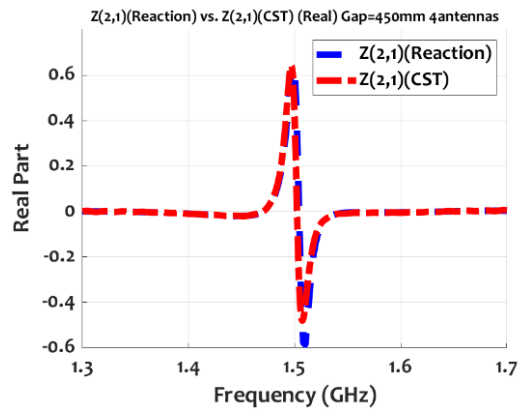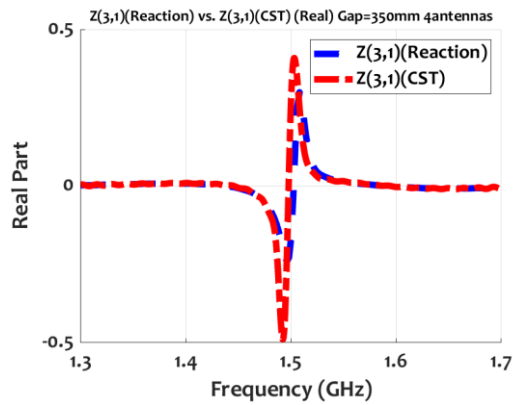
Figure 4.84: Z(3,1) Real Part Comparison for 4 Antennas with 350mm spacing and a Sphere Target
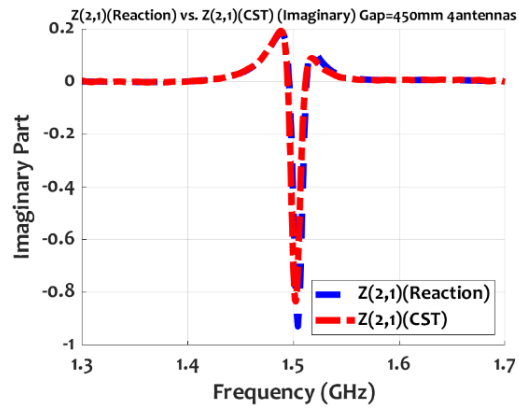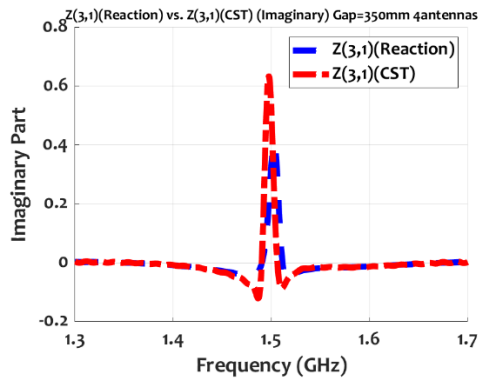

Figure 4.85: Z(3,1) Imaginary Part Comparison for 4 Antennas with 350mm spacing and a Sphere Target

By observing Figure 4.83 - Figure 4.85 it can be said that accuracy degrades as the antennas gets closer and Z-parameter results for 4 antenna scenario are not as accurate as 2 antenna case. To understand whether this degradation is caused by the presence of other antennas, another CST simulation is run where antenna 2 and antenna 4 are removed from simulation scenario and mutual impedance between antenna 1 and antenna 3 are simulated and added to the comparison. Results are given in Figure 4.86 - Figure 4.88.
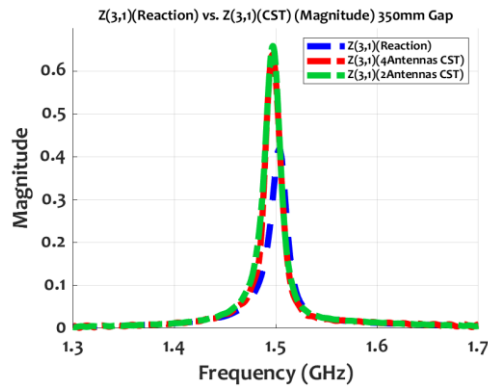
Figure 4.86: Z(3,1) Magnitude Comparison by removing 2 antennas
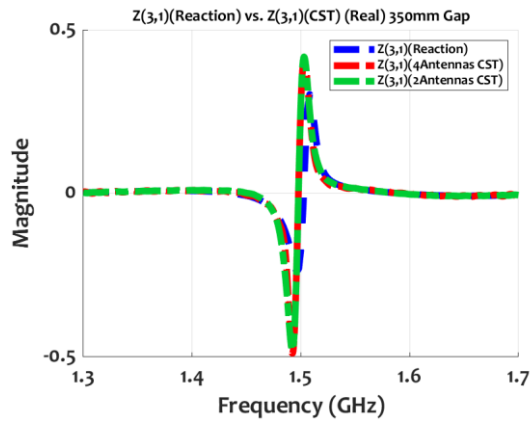
Figure 4.87: Z(3,1) Real Part Comparison by removing 2 antennas
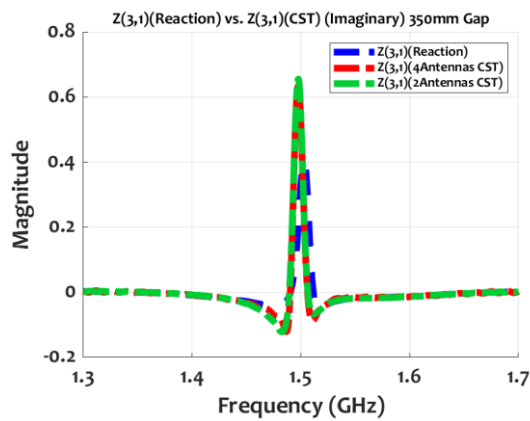
Figure 4.88: Z(3,1) Imaginary Part Comparison by removing 2 antennas

Results of CST Microwave Studio shows that presence of other antennas has negligible impact on mutual impedance between transmitter and receiver antenna.

Hence, we can say that when antennas are getting closer to each other, assumption made in the proposed method starts to be invalid and the method provides less accurate results compared to CST. On the other hand, based on this last simulation it can be concluded that increasing the number of antennas in the array does not affect the mutual impedance between the transmitter and receiver antennas and this is a favorable observation for the proposed method. Because as it will be discussed below, the computational cost of the proposed method increases slightly with the number of antennas whereas it increases substantially in CST simulations.

Simulation scenario in Figure 4.72 took 1 hour, 56 minutes and 45 seconds with 12-core processor by using CST Microwave Studio. However, by using the proposed method, finding the mutual impedances between two antennas takes 3 minutes and 34 seconds in total. This process must be repeated for 6 times to find mutual impedance between every antenna pair so a total simulation would take 21 minutes and 24 seconds. Advantage for simulation time will increase as the domain gets larger since CST needs to run simulation for a larger domain, whereas simulation time for the proposed method is independent of the number of antennas for the computation of 1 mutual impedance value for a couple of antennas.

CHAPTER 5

CONCLUSION

In this thesis, a fast simulation and modeling method is proposed for MIMO imaging systems. Since, finding the optimal placement and design is time-consuming with traditional full-wave simulations, aim of this work was creating such a method that is faster and more-flexible without sacrificing accuracy. To construct such a method, it is proposed to analyze transmitter antenna, receiver antenna and the target seperately. Surface equivalence theorem and small dipole approximation is employed in order to calculate incident fields at any arbitrary point in the problem domain for each frequency. To employ these mentioned approaches, result of a full-wave simulation of one of the antennas is required. Altough this process adds up to simulation time, it will require considerably less amount of time compared to a full-wave simulation that includes the whole system. It should be also noted that, mentioned full-wave simulation needed to be run only once, so as the number of antennas in the system increases, impact of the first full-wave simulation within the total simulation time decreases. In Chapter 3, MoM technique is employed to compute the scattered fields from the target. For the same target, as the position of the transmitter antenna changes, the impedance matrix [Z] in MoM remains same, so only the induced current coefficients need to be solved for the new voltage excitation vector [V]. Finally in Chapter 4, Reaction Theorem and its application is explained to find the interaction between transmitter antenna and receiver antenna in the presence of the target. In Chapter 4, through a couple of numerical examples it is demonstrated that the proposed method provides quite accurate results with considerably reduced computational cost and memory allocation compared to full-wave analysis of the whole structure. However, the distance between the antennas is found to be the most critical parameter for the accuracy of the proposed method. As a future work, more detailed analysis will be performed to investigate the sources of

error when antennas get closer. After finding these error sources, modifications to the proposed method can be developed to improve accuracy for closer antenna placements.

REFERENCES

[1] Xiaodong Zhuge and Alexander G. Yarovoy, "A Sparse Aperture MIMO-SAR-Based UWB Imaging System for Concealed Weapon Detection," *IEEE Transactions on Geoscience and Remote Sensing,* vol. 49, no. 1, 2011.

[2] Xiadong Zhuge and Alexander Yarovoy, "MIMO-SAR," in *8th European Conference on Synthetic Aperture Radar*, 2010.

[3] Fulai Liang, Miao Liu; Haonan Li, Fugui Qi, Zhao Li and Jianqi Wang, "Through-the-wall imagery of human vital signs using UWB MIMO bioradar," in *ITNEC*, 2017.

[4] T. Sakamoto, "Noncontact Measurement of Human Vital Signs during Sleep Using Low-power Milimeter-wave Ultrawideband MIMO Array Radar," in *IMBioC*, 2019.

[5] Milan M. Ilic, Miroslav Djordjevic, Andjelija Z. Ilic, and Branislav M. Notaros, "Higer Order Hybrid FEM-MoM Technique for Analysis of Antennas and Scatterers," *IEEE Trans. Antennas and Propagation,* vol. 57, no. 5, pp. 1452-1460, 2009.

[6] Andre Barka and Pierre Caudriller, "Domain Decmoposition Method Based on Generalized Scattering Matrix for Installed Perofmrance of Antennas on Aircraft," *IEEE Trans. Antennas and Propagation,* vol. 55, no. 6, pp. 1833-1841, 2007.

[7] Miroslav Djordjevic and Branislav M. Notaros, "Higher Order Hybrid Method of Moments-Physical Optics Modeling Technique for Radiation and Scattering Fromt Large Perfectly Conducting Surfaces," *IEEE Trans. Antennas and Propagation,* vol. 53, no. 2, pp. 800-813, 2005.

[8] Tian-Qi Fan, Li-Xin Guo and Wei Liu, "A Novel OpenGL-Based MoM/SBR Hybrid Method for Radiation Pattern Analysis of an Antenna Above an Electrically Large Complicated Platform," *IEEE Trans. Antennas and Propagation,* vol. 64, no. 1, pp. 201-209, 2016.

[9] Benoit Le Lepriver, Renaud Loison, Raphael Gillard, Philippe Poulingen, Patrick Potier, and Laurent Patier, "A New Hybrid Method for the Analysis of Surrounded Antennas Mounted on Large Platforms," *IEEE Trans. Antennas and Propagation,* vol. 62, no. 5, pp. 2388-2397, 2014.

[10] Kezhong Zhao, Vineet Rawar, Jin-Fa Lee, "A Domain Decomposition Method for Electromagnetic Radiation and Scattering Analysis of Multi-Target Problems," *IEEE Trans. Antennas and Propagation,* vol. 56, no. 8, pp. 2211-2221, 2008.

[11] A. Barka, "Integration of Antennas Onbard Vehicles and Diffraction by Large and Complex Structres With Multiple-Domain-Multiple-Methods Techniques," *Proceedings of the IEEE,* vol. 101, no. 2, pp. 280-297, 2013.

[12] Mark Kragalott, Michael S. Klukens, Dale A. Zolnick, W. Mark Dorsey, and John A. Valenzi, "A Toolset Independent Hybrid Method for Calculating Antenna Coupling," *IEEE Trans. Antennas and Propagation,* vol. 59, no. 2, pp. 443-451, 2011.

[13] Si-Ping Gao, Huapeng Zhao, Hong-Wei Deng, Bin-Fang Wang, and Wei-Jiang Zhao, "Estimating Interference to Airborne Patch Antenna With Limited Information," *IEEE Transactions on Electromagnetic Compatiblity,* vol. 58, no. 2, pp. 631-634, 2016.

[14] Johan Lundgren, Johan Malmström, Jari-Matti Hannula, and B. L. G. Jonsson, "Visualization and Reduction of Mutual Coupling Between

Antennas Installed on a Platform," *IEEE Transactions on Electromagnetic Compatibility,* vol. 64, no. 1, pp. 92-101, 2022.

[15] Hanfeng Wang, Victor Khilkevich, Yao-Jiang Zhang, and Jun Fan, "Estimating Radio-Frequency Interference to an Antenna Due to Near-Field Coupling Using Decomposition Method Based on Reciprocity," *IEEE Transaction on Electromagnetic Compatibility,* vol. 55, no. 6, pp. 1125-1131, 2013.

[16] S. A. Schelkunoff, "Some equivalence theorems of electromagnetics and their application to radiation problems," *Bell System Tech J.,* vol. 15, pp. 92-112, 1936.

[17] A. Love, "The integration of the equationf of propagation of electric waves," *Phil.Trans.Roy. Soc London,* vol. 197, pp. 1-45, 1901.

[18] C. A. Balanis, Advanced Electromagnetics 2nd Edition, John Wiley & Sons, Inc., 2012.

[19] C. A. Balanis, Antenna Theory 3rd Edition, New Jersey: John Wıley & Sons Inc., 2005.

[20] J.D.Kraus, Electromagnetics, New York: McGraw Hill, 1950.

[21] A.F Peterson, S.L. Ray and R. Mittra, "Computational Methods for Electromagnetics," *IEEE Press,* 1998.

[22] S.M Rao, D.R. Wilton and A.W. Glisson, "Electromagnetic scattering by surfaces of arbitrary shape," *IEEE Trans. Antennas and Propagation,* pp. 409-418, 1982.

[23] Y. Kamen and L. Shirman, "Triangle rendering using adaptive subdivision," *IEEE Computer Graphics and Applications,* pp. 95-103, 1998.

[24] S. N. Makarov, Antenna and EM Modeling with MATLAB, New York: John Wiley & Sons Inc., 2002.

[25] J. Carson, "Reciprocal theorems in radio communication," *PROC. IRE,* vol. 17, pp. 952-956, 1929.

[26] V. Rumsey, "Reaction concept in electromagnetic theory," *Phys. Rev.,* vol. 94, pp. 1483-1491, 1954.

[27] R. G. Kouyoumijan, "The Calculation of the Echo Areas of Perfectly Conducting Objects by Variational Merhod," *Antenna Lab., Ohio State Univ. Res. Foundation, Columbus, Rept.,* no. 444, pp. 80-84, 1953.

[28] J. Richmond, "A Reaction Theorem and Its Application to Antenna Impredance Calculations," *IRE Transactions on Antennas and Propagation,* pp. 515-520, 1961.

[29] J. Malmström, "On the Reaction Theorem for Scattered Fields," *IEEE Antennas and Wireless Propagation Letters,* 2017.